

# Computational Characterization of a Millimeter-Wave Heat Exchanger with AlN:Mo Cylindrical Susceptors

A Major Qualifying Project (MQP) Report  
Submitted to the Faculty of  
WORCESTER POLYTECHNIC INSTITUTE  
in partial fulfillment of the requirements  
for the Degree of Bachelor of Science in

Mathematical Sciences,  
Physics

By:

Catherine M. Hogan

Project Advisors:

Professor Vadim V. Yakovlev, WPI  
Professor Alex A. Zozulya, WPI

Sponsored By:

Air Force Research Laboratory

Date: May 2021

*This report represents work of WPI undergraduate students submitted to the faculty as evidence of a degree requirement. WPI routinely publishes these reports on its website without editorial or peer review. For more information about the projects program at WPI, see <http://www.wpi.edu/Academics/Projects>.*

# Abstract

Electromagnetic (EM) heating has traditionally been applied in fields such as food engineering, chemistry, and materials science. More recently, a new field of EM heating has emerged for applications in power beaming technology. The EM heat exchangers (HX) are used in beamed energy propulsion, solar thermal collectors, and wireless energy transfer.

A new type of EM HX for ground-to-ground millimeter-wave (MMW) power beaming applications has been recently introduced by the US Air Force Research Laboratory (AFRL). This device is comprised of an array of ceramic susceptors attached to a metal baseplate along the back surface. An incident wave is projected onto the ceramic elements, which absorb the EM power and are heated up, subsequently heating up the attached baseplate. Fluid channels housed in the baseplate are then used to carry the heat away. Computer modeling of the MMW HX with a susceptor made as a single rectangular block of a ceramic composite (aluminum nitride doped with molybdenum, AlN:Mo) has recently shown elevated energy efficiency and high level of uniformity of the temperature field in the ceramic block. Currently, the further development of a MMW HX device which utilizes cylindrical susceptors is of particular interest, due to the practicality and cost of production.

In this MQP, we present results of numerical computations that demonstrated feasibility of the design of the experimental system made of five AlN:Mo cylinders on a square metal plate. Simulation of the EM and thermal processes is performed via the 3D finite-difference time-domain technique implemented in the simulator *QuickWave*. It is shown that while the energy efficiency of this system depends on the concentration of molybdenum doping in the composite, all concentrations provide sufficiently high temperature distribution.

Computations are also made for the systems whose layouts are suggested by the highest density packing of equal circles in a square and feature four, nine and sixteen cylinders. We show that, in each of the various multi-cylinder models, a maximum energy efficiency can be achieved with different concentrations of Mo, whereas all concentrations provide excellent uniformity of temperature distribution within each ceramic cylinder.

The results of this project are being adopted by the AFRL, Kirtland, AFB, NM as supporting data in the experiments with the new MMW HX for ground-to-ground wireless power transfer.

# Acknowledgements

I would like to thank the following people who have aided me immensely in the completion of this project, and whose work on further research will develop this project beyond the work I have done:

- Professor Vadim V. Yakovlev, Worcester Polytechnic Institute, Worcester, MA - for the opportunity to join this research team, and for serving as my project advisor and offering assistance and advice given at every step;
- Professor Alex A. Zozulya, Worcester Polytechnic Institute, Worcester, MA - for serving as my project advisor and offering advice along the way;
- Dr Brad Hoff and his team at the Air Force Research Laboratory, Kirtland Air Force Base, Albuquerque, NM - for sponsoring this project;
- Professor Burt S. Tilley, Worcester Polytechnic Institute, Worcester, MA - for introducing me to this project and serving as my major advisor for all four years at WPI;
- and everyone who has worked on this project before me and everyone who will continue to work on this project when my portion is complete.

# Contents

<b>1</b>	<b>Introduction</b>	<b>1</b>
1.1	Background . . . . .	1
1.2	Previous Studies . . . . .	3
1.3	Project Objectives . . . . .	4
<b>2</b>	<b>Methodology</b>	<b>5</b>
<b>3</b>	<b>Development of FDTD Models</b>	<b>7</b>
3.1	Model with Vertical Propagation of the Plane Wave . . . . .	7
3.2	Models with Cylindrical Susceptors . . . . .	10
<b>4</b>	<b>Computation of Energy Efficiency</b>	<b>13</b>
4.1	Energy Efficiency of Multi-Cylinder Systems . . . . .	13
4.2	Electromagnetic Fields of the Five-Cylinder Model . . . . .	15
<b>5</b>	<b>Computation of Temperature Fields</b>	<b>16</b>
5.1	Five-Cylinder Systems: Heating Rates . . . . .	16
5.2	Multi-Cylinder Models: Temperature Patterns . . . . .	16
<b>6</b>	<b>Supplementary Topics</b>	<b>20</b>
6.1	Susceptors with a Dielectric Topping . . . . .	20
6.2	Off-Normal Incidence . . . . .	21
6.3	Thermal Boundary Conditions . . . . .	22
<b>7</b>	<b>Conclusion</b>	<b>24</b>
	<b>Appendices</b>	<b>25</b>
<b>A</b>	<b>UDO Scripts for <i>QuickWave</i> Models with Cylindrical Susceptors</b>	<b>25</b>
<b>B</b>	<b>Temperature Field Patterns in Five-Cylinder Model</b>	<b>43</b>
<b>C</b>	<b>Calculation of Exposed Surface Areas Based on Angle of Incidence</b>	<b>47</b>
<b>D</b>	<b>Exposed Surface Area MATLAB Script</b>	<b>52</b>
<b>E</b>	<b>Computational Tests of Thermal Boundary Conditions</b>	<b>54</b>
<b>F</b>	<b>Determining Convective Heat Transfer Coefficient</b>	<b>58</b>
<b>G</b>	<b>Plane Wave Incidence Settings in <i>QuickWave</i></b>	<b>61</b>
	<b>References</b>	<b>62</b>



# List of Tables

- 1.1 Dielectric (at 95 GHz) and Thermal Properties of AlN:Mo Composite at the End-points of the MMW HX Operating Temperature Interval . . . . . 4
- F.1 Material Properties Used in Determining Convective Heat Transfer Coefficient . . . . . 59

# List of Figures

1.1	Concept of wireless power transfer. . . . .	2
1.2	Concept of the AFRL’s MMW HX. . . . .	2
1.3	Scenario with a single “horizontal” cube. . . . .	3
1.4	BeO, AlN, and Al <sub>2</sub> O <sub>3</sub> : ceramic materials with highest thermal conductivities. . . . .	3
2.1	The FDTD algorithm for solving a coupled EM-thermal problem in <i>QuickWave</i> , in accordance with [27-31]. . . . .	6
3.1	Patterns of dissipated power density in “horizontal” AlN:Mo cube. . . . .	8
3.2	Patterns of dissipated power density in “vertical” AlN:Mo cube. . . . .	8
3.3	Mesh before adjustments in “horizontal” (a) and “vertical” (b) cubes. . . . .	9
3.4	Mesh after adjustments in “horizontal” (a) and “vertical” (b) cubes. . . . .	9
3.5	AFRL’s design of MMW HX with five cylindrical susceptors. . . . .	10
3.6	Model of the MMW HX physical prototype: five cylinders on a metal plate; normal or off-normal plane wave incidence from the top. . . . .	10
3.7	Basic cylindrical FDTD model. . . . .	11
3.8	Five-cylinder FDTD model. . . . .	11
3.9	Four-cylinder FDTD model. . . . .	12
3.10	Nine-cylinder FDTD model. . . . .	12
3.11	Sixteen-cylinder FDTD model. . . . .	12
4.1	Energy efficiency (at different temperatures of the AlN:Mo composite and average) of the experimental five-cylinder system; normal incidence ( $\theta = 0$ ); red points characterize the system with one rectangular AlN:Mo block. . . . .	14
4.2	Energy efficiency (at different temperatures of the AlN:Mo composite and average) of the experimental four-cylinder system; normal incidence ( $\theta = 0$ ). . . . .	14
4.3	Energy efficiency (at different temperatures of the AlN:Mo composite and average) of the experimental nine-cylinder system; normal incidence ( $\theta = 0$ ). . . . .	14
4.4	Relative patterns of the electric field envelopes in the vertical ( $xz$ -) planes through the five-cylinder system for different concentrations of Mo in the composite susceptors. . . . .	15
5.1	Maximum and minimum temperatures throughout the five-cylinder system. . . . .	17
5.2	Time evolution of the temperature field in the vertical ( $xz$ -) plane through the two edge susceptors (a) and in the central horizontal ( $xy$ -) plane through the all susceptors (b) with Mo = 0.25, . . . , 4.0% in the five-cylinder model. . . . .	18
5.3	Time evolution of the temperature field in the vertical ( $xz$ -) plane through the two edge susceptors and in the central horizontal ( $xy$ -) plane through the all susceptors with Mo = 3.0% in the four-cylinder model. . . . .	19

5.4	Time evolution of the temperature field in the vertical ( $xz$ -) plane through the two edge susceptors and in the central horizontal ( $xy$ -) plane through the all susceptors with Mo = 3.0% in the nine-cylinder model. . . . .	19
6.1	Model of a single cylinder with pointed top. . . . .	21
6.2	Energy efficiency of the single-cylinder system with an AlN:Mo cone on the top surface at different heights of the cone; normal incidence ( $\theta = 0$ ). . . . .	21
6.3	Five-cylinder FDTD model with off-normal plane wave incidence with inclination along the $x$ -axis (a) and $y$ -axis (b) . . . . .	22
B.1	Temperature scale for patterns of temperature distribution in AlN:Mo susceptors. . .	43
B.2	Temperature patterns in the $xy$ -plane along the surface adjacent to the baseplate (a) and in the $xz$ -plane (b) for 0.25% Mo. . . . .	44
B.3	Temperature patterns in the $xy$ -plane along the surface adjacent to the baseplate (a) and in the $xz$ -plane (b) for 0.5% Mo. . . . .	44
B.4	Temperature patterns in the $xy$ -plane along the surface adjacent to the baseplate (a) and in the $xz$ -plane (b) for 1.0% Mo. . . . .	45
B.5	Temperature patterns in the $xy$ -plane along the surface adjacent to the baseplate (a) and in the $xz$ -plane (b) for 2.0% Mo. . . . .	45
B.6	Temperature patterns in the $xy$ -plane along the surface adjacent to the baseplate (a) and in the $xz$ -plane (b) for 3.0% Mo. . . . .	46
B.7	Temperature patterns in the $xy$ -plane along the surface adjacent to the baseplate (a) and in the $xz$ -plane (b) for 4.0% Mo. . . . .	46
C.1	Four-cylinder model with incidence angle $\theta$ : no overlap in exposed surface area (a); some overlap in exposed surface area (b). . . . .	48
C.2	Exposed surface area of single cylinder with incidence angle $\theta$ : view of the side (a); view of the top from incidence angle $\theta$ (b). . . . .	49
C.3	Exposed surface area of two overlapping cylinders with incidence angle $\theta$ : view of the side (a); view of the top from incidence angle $\theta$ (b). . . . .	49
C.4	Exposed surface area of multi-cylinder models as a function of angle of incidence. . .	50
E.1	Temperature patterns in the zirconia cube on the $xz$ -plane through center. . . . .	55
E.2	Temperature patterns in the zirconia cube on the $yz$ -plane through center. . . . .	55
E.3	Temperature patterns in the zirconia cube on the $xz$ -plane on right face with adiabatic (a) and explicit (b) BCs. . . . .	56
E.4	Temperature patterns in the zirconia cube on the $yz$ -plane on front face with adiabatic (a) and explicit (b) BCs. . . . .	56
E.5	Temperature patterns in the zirconia cube on the $xy$ -plane adjacent to metal plate (normalized to 324°C). . . . .	57
E.6	Temperature patterns in the zirconia cube on the $xy$ -plane adjacent to metal plate (normalized to respective $T_{max}$ ). . . . .	57

F.1	Microsoft Excel spreadsheet which, in accordance with Table F.1, inputs the AlN:Mo material parameters $\rho = 1.17 \frac{kg}{m^3}$ , $g = 9.81 \frac{m}{s^2}$ , $T = 300K$ , $\beta = 0.0333K^{-1}$ , $\mu = 1.40 \cdot 10^{-5} Pa s$ , $c_p = 1000 \frac{J}{kgK}$ , $k = 0.02 \frac{W}{mK}$ , $\alpha = 1.71 \cdot 10^{-5} \frac{m^2}{s}$ , $H = 0.1m$ , and $T_s = 500K$ to produce the values $Pr = 0.700$ , $Ra = 3.20 \cdot 10^7$ , and, finally, $h = 8.71 \frac{W}{m^2K}$	60
G.1	Plane wave incidence settings in <i>QuickWave</i> . . . . .	61

# 1 Introduction

## 1.1 Background

Electromagnetic (EM) heating has traditionally been applied in fields such as food engineering, chemistry, and materials science. More recently, a new field of EM heating has emerged for applications in power beaming technology. The EM heat exchangers (HX) are used in thermal thrusters employing EM energy to produce thrust by thermal expansion of a compressed gas [1], beamed energy propulsion [2, 3], solar thermal collectors [4], and wireless energy transfer [5–9].

A new type of EM HX has been recently introduced by the US Air Force Research Laboratory (AFRL) for ground-to-ground millimeter-wave (MMW) power beaming applications. In this technology, an EM wave is generated at one location and transmitted to another location, where the wave is absorbed by a receiving system and used to generate energy (Figure 1.1). With an intent to make contribution to the AFRL development, this project focuses on the receiving systems, which is an MMW HX [10–16]. Figure 1.2 shows this device comprised on an array of ceramic absorbing elements (susceptors) attached to a metal baseplate. The EM wave is absorbed by the ceramic susceptors which, in their turn, heat up the baseplate. The thermal energy is then carried away by fluid (or gas) running through channels in the baseplate to be converted into mechanical energy. Theoretical studies behind this concept show a potential for high efficiency of layered structures due to a possible resonance-based control over thermal runaway [9, 16, 17]. A computer model of the MMW HX with a susceptor made as a single rectangular block of a ceramic composite (aluminum nitride doped with molybdenum, AlN:Mo) [13] has shown elevated energy efficiency and high level of uniformity of the MMW-induced temperature field in the ceramic block. The promising results from this model have supported further development of the MMW HX device. A MMW HX device

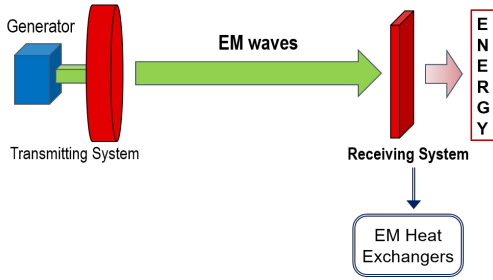


Figure 1.1: Concept of wireless power transfer.

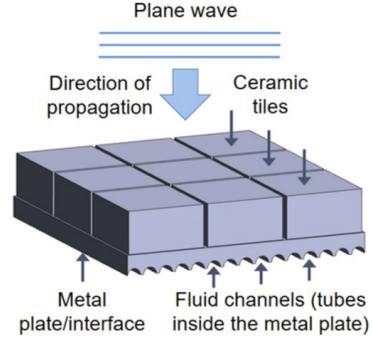


Figure 1.2: Concept of the AFRL's MMW HX.

which utilizes cylindrical susceptors is of particular interest, due to the practicality and cost of production of the composite absorbing elements in comparison to the cubic designs.

In this MQP, we develop computer models of a series of MMW HX with cylindrical susceptors and perform simulations of EM and thermal processes in order to better understand interaction between the MMW and the absorbing elements, identify beneficial compositions of the AlN:Mo, and help design the physical prototype of the device. Simulation is performed via the 3D finite-difference time-domain (FDTD) technique implemented in the simulator *QuickWave* [18].

We present computational analysis demonstrating feasibility of the AFRL design of the experimental system made of five AlN:Mo cylinders on a square metal plate. We show that while the energy efficiency of this system depends on the concentration of molybdenum doping in the composite, all concentrations tested have shown sufficiently high EM-induced temperature distribution. The results of the five-cylinder model are then compared with models whose layouts are suggested by the highest density packing of equal circles in a square [19–21] and feature four, nine and sixteen cylinders. Our computational results suggest that, in each of the various multi-cylinder models, a maximum energy efficiency can be achieved with different concentrations of molybdenum, and shows that all concentrations provide excellent uniformity of temperature distribution within each ceramic cylinder of the system.

Overall, this report demonstrates usefulness of numerical modeling for the simulation of EM characteristics of the MMW HX and volumetric temperature fields in the ceramic suscep-

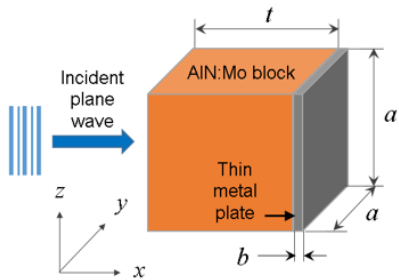


Figure 1.3: Scenario with a single “horizontal” cube.

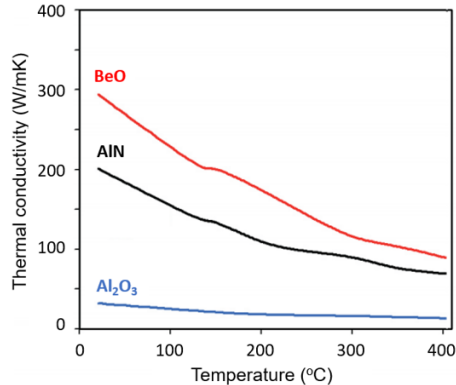


Figure 1.4: BeO, AlN, and Al<sub>2</sub>O<sub>3</sub>: ceramic materials with highest thermal conductivities.

tors. The computer models built in this MQP are meant to be tools directly assisting in further development of the concept and supporting system design of the new MMW HX.

## 1.2 Previous Studies

The earlier modeling projects were concerned with a single cubic susceptor, pictured in Figure 1.3. The EM and thermal processes of this MMW HX are reported in [12–15]. This model was arbitrarily built in *QuickWave* so that the direction of propagation of the plane wave and orientation of the device do not allow for simple modifications to more complex layouts, including those with cylindrical susceptors. This MQP, therefore, presents a series of new models built with an alternative orientation of the device.

The susceptors in the MMW HX models are made up of a ceramic composite based on aluminum nitride, which was chosen for its high thermal conductivity, having the second highest of any known ceramic materials (Figure 1.4, adapted from [22]). The AlN was also doped with various levels of molybdenum (Mo) with an expectation to control its dielectric properties, and thus potentially optimize the performance of the HX. Temperature-dependent EM and thermal parameters of AlN:Mo are given in [13] as generalization of experimental data reported in [23–26]. Material parameters of the AlN:Mo with six different Mo concentrations, ranging from 0.25% to 4.0% (by volume), includes dielectric constant ( $\epsilon'$ ) and the loss factor ( $\epsilon''$ ) (at 95GHz) as well

Table 1.1: Dielectric (at 95 GHz) and Thermal Properties of AlN:Mo Composite at the Endpoints of the MMW HX Operating Temperature Interval

Mo (%)	Temperature (°C)	$\epsilon'$	$\epsilon''$	$\rho$ (g/cm <sup>3</sup> )	$c_p$ (J/gC)	$k$ (W/cmC)
0.25	20	8.61	0.029	3.32	0.702	1.403
	1000	9.40	0.068		1.142	0.385
0.5	20	8.76	0.036	3.33	0.704	1.242
	1000	9.54	0.085		1.142	0.425
1.0	20	9.09	0.050	3.37	0.692	1.300
	1000	9.88	0.099		1.136	0.390
2.0	20	9.96	0.120	3.44	0.681	1.375
	1000	10.94	0.198		1.129	0.349
3.0	20	11.48	0.465	3.50	0.668	1.374
	1000	12.66	0.661		1.123	0.359
4.0	20	13.45	1.167	3.57	0.658	1.345
	1000	14.73	1.559		1.124	0.362

as specific heat ( $c_p$ ) and thermal conductivity ( $k$ ) are listed in Table 1.1 for the temperature interval from 20 to 1,000°C [13]. Because the material parameters of the AlN and the AlN:Mo are temperature dependant, data on the material parameters in the entire temperature range is absolutely necessary as input data for the computer model built and used in this project.

### 1.3 Project Objectives

This project therefore focuses on three primary tasks:

1. Develop a series of new models for *QuickWave* that can be used in computational tests of the MMW HXs with cylindrical susceptors.
2. Use these models to evaluate energy efficiency and find the material for the cylindrical susceptors which best absorbs the incident EM waves.
3. Simulate temperature patterns induced by the EM field and evaluate the level of heating uniformity within the cylindrical susceptors of the MMW HXs.



## 2 Methodology

Computational experiments were conducted based on the multiphysics simulation coupling the EM and thermal phenomena occurring in the HX with AlN:Mo cylindrical susceptors irradiated by high-power MMW. The models employed in the present study were built as modifications of the EM-thermal model [13] for a rectangular AlN:Mo block of a metal plate that was described in detail and verified against the model of the same system built in *COMSOL Multiphysics*. The simulations were carried out with the 3D conformal finite-difference time-domain (FDTD) technique implemented in *QuickWave* [18].

In the coupled simulation, the EM and thermal solvers operate as parts of an iterative procedure [27–31] in which a steady state solution of the EM problem becomes an input for the thermal problem, illustrated in Figure 2.1. The heating occurs for the time specified in the set heating time step  $\delta t$ , after which the process returns to the EM solver. In all subsequent runs of the EM solver, material parameters are upgraded in every cell of the applied FDTD mesh in accordance with the temperature field outputted from the thermal solver. The latter determines temperature formed in the absorbing material after each  $\delta t$ ; after a certain number of iterations, maximum temperature of the process (not exceeding the maximum value in the data on temperature-dependent material parameters) is reached, and the solution process stops.

In the implementation of the open scenario in a finite-size FDTD model, the system is surrounded by a plane wave box with the face on the top responsible for excitation of the incident plane wave. This box, in its turn, is situated inside a rectangular space whose boundaries imitate the Mur superabsorbing boundary condition [18].

Following the steps in the model in [13], to satisfy the FDTD stability criterion and

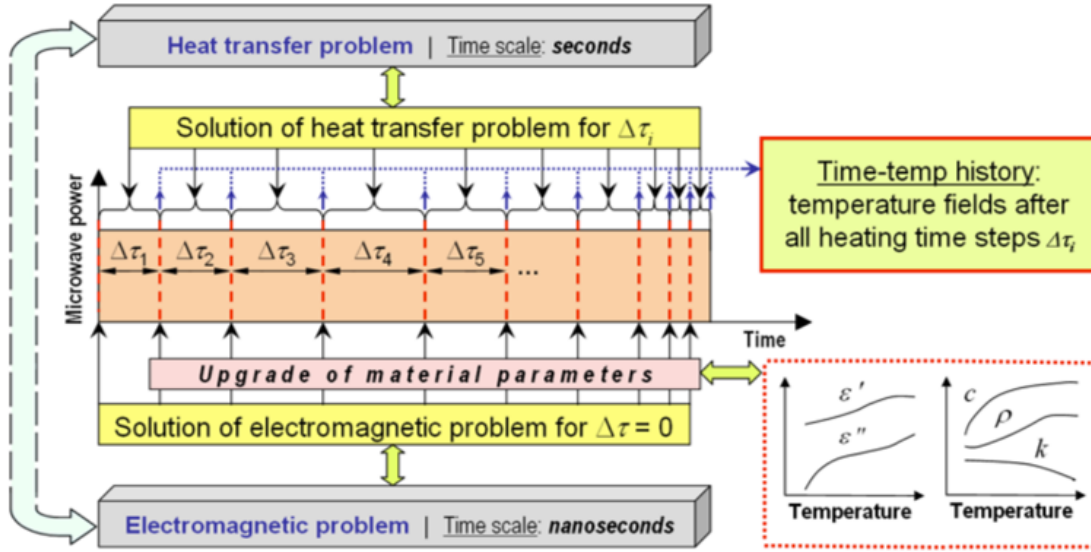


Figure 2.1: The FDTD algorithm for solving a coupled EM-thermal problem in *QuickWave*, in accordance with [27-31].

minimize computational resources, the scenario is discretized with the mesh with maximum cell sizes of 0.29mm (in air) and from 0.075 to 0.095mm (in the ceramic composite, in accordance with dielectric constants  $\epsilon'$  related to  $Mo = 4\%$  ( $\epsilon' = 14.73$ ) and 0.25%, ( $\epsilon' = 9.54$ ) and the highest temperature of 1,000°C, respectively).

In this report, simulations were performed on a Window 10 workstation with two Intel Xeon Gold 5120 processors with a base/peak frequency of 2.2/3.2 GHz (each having 14 cores and supporting 28 threads), the GPU NVIDIA Quadro P5000 and 1 TB RAM.

## 3 Development of FDTD Models

### 3.1 Model with Vertical Propagation of the Plane Wave

In *QuickWave*, 3D structures are (conceptually and practically) created by expanding 2D objects located in the “horizontal”  $xy$ -plane along the perpendicular  $z$ -axis. This means that in rational resource-saving models circular cylinders would be naturally oriented along the  $z$ -axis. In the context of the MMW HX design, that requires that the plane wave irradiating the cylindrical objects would travel also along the  $z$ -axis. However, in the earlier *QuickWave* models [12,13,15] developed for the study of MMW HX with a single rectangular (cubic) susceptor, the direction of propagation of the plane was arbitrarily chosen along the  $x$ -axis.

To fulfill the conditions applied by the principles of generation of 3D objects in *QuickWave*, the new models with “vertical” orientation of the cylindrical objects had to be created. To guarantee the adequacy and accuracy of the new models, at the first step, the model with a single cubic susceptor was revised for the “vertical” direction of propagation of the plane wave. Since the results of the “horizontal” model were verified against the output of alternative numerical computations (by finite element method in *COMSOL Multiphysics*) [13,15], it was necessary to verify that modeling results from both “horizontal” and “vertical” models with the cubic susceptor are identical. The second step then would be reduced to a replacement of this single block by a series of cylindrical objects.

The tests to compare the “horizontal” and “vertical” single cube models used the composites with three of the six concentrations of Mo: 0.5, 1.0, and 3.0%. For each combination of orientation and concentration, the simulation ran for 10 000 FDTD time steps in order to allow for the computation to reach steady state. Once the simulations reached 10 000 time steps, the

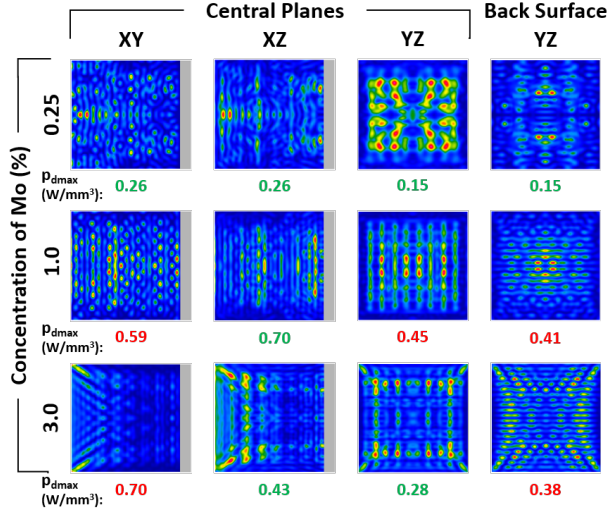


Figure 3.1: Patterns of dissipated power density in “horizontal” AlN:Mo cube.

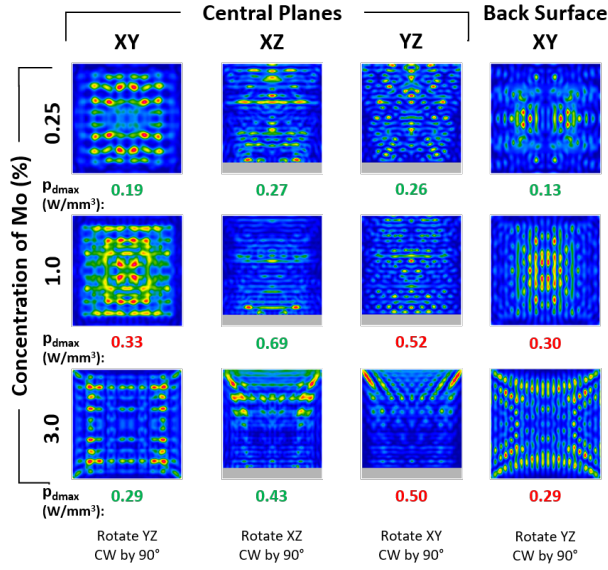


Figure 3.2: Patterns of dissipated power density in “vertical” AlN:Mo cube.

patterns of dissipated power density and maximum values were collected for four different planes: the plane adjacent to the metal plate ( $yz$ -plane for “horizontal” model,  $xy$ -plane for “vertical” model), and the  $xy$ -,  $xz$ -, and  $yz$ -planes through the center of the cube. Figures 3.1 and 3.2 show the patterns and maximum values of all four planes in both the “horizontal” and “vertical” models for the three different concentrations of Mo. Values written in red are values with discrepancies

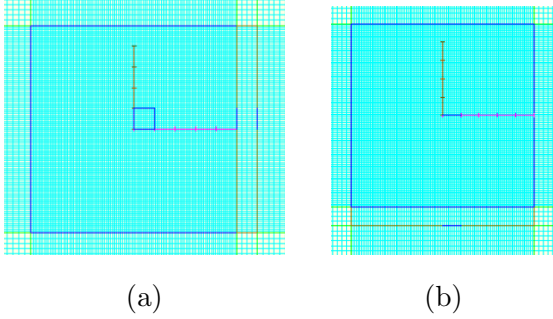


Figure 3.3: Mesh before adjustments in “horizontal” (a) and “vertical” (b) cubes.

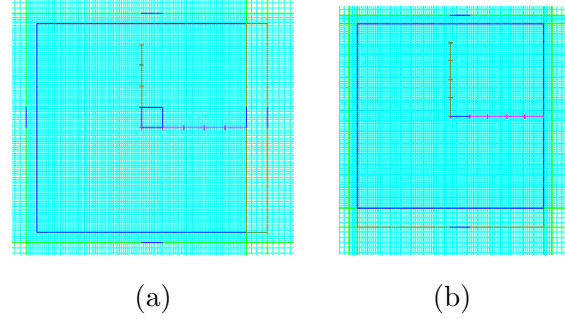


Figure 3.4: Mesh after adjustments in “horizontal” (a) and “vertical” (b) cubes.

between the two models, while values written in green are identical or near-identical. Because of the changes in orientation, Figure 3.2 also indicates which planes correspond to the planes pictured in Figure 3.1.

When comparing the “horizontal” and “vertical” models of a single AlN:Mo cube, there were discrepancies in five out of the twelve corresponding values recorded during testing. From a special investigation, it was found that these discrepancies were caused by the properties of the mesh (or FDTD cell patterns) used in the model. The FDTD method in *QuickWave* assigns material parameters (components in all three directions) to each cell with reference to the position of field components in the FDTD cell. Material parameters at the boundary (where the ceramic block interfaces the air or the metal plate) are an average between parameters of the two materials. These averages take into account the cell sizes at the boundary, and if a significant step in cell size is present where the air cell is larger than the ceramic cell, material parameters at the boundary will be lower in comparison to at the center of the cube. This averaging effect is slightly different in the two models, causing slightly different diffraction effects and producing the discrepancies. Initially, the cell size changed directly at the boundary (Figure 3.3). To reduce the impact of the averaging effect on the results, the mesh was adjusted at the boundaries, so that the cell size didn’t increase until 0.5 mm beyond the boundary (Figure 3.4).

Following the adjustments to the mesh parameters, the tests to compare the two models were run again and the discrepancies had been fully eliminated. All patterns and values for maximum dissipated power density were identical or near-identical across the two models in each

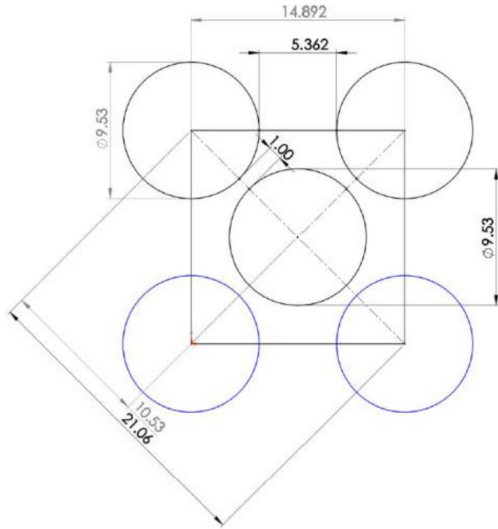


Figure 3.5: AFRL's design of MMW HX with five cylindrical susceptors.

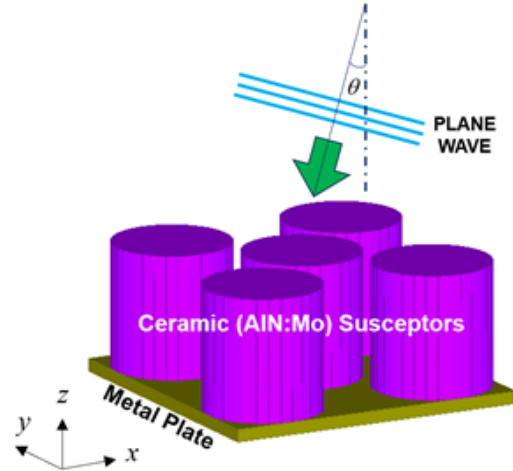


Figure 3.6: Model of the MMW HX physical prototype: five cylinders on a metal plate; normal or off-normal plane wave incidence from the top.

plane for all concentrations tested. Therefore, all future models developed included the 0.5 mm gap between the boundaries and the change in cell size to minimize the impact of the averaging effect on the results.

## 3.2 Models with Cylindrical Susceptors

With confirmation that the orientation of the model of the MMW HX and propagation of the plane wave has little to no impact on the results of the simulation, more complex models made. The first one represents a five-cylinder scenario with a single cylinder in the center of the square metal baseplate and one cylinder in each of the four corners. The plan provided by the AFRL, pictured in Figure 3.5 and represented in 3D in Figure 3.6, proposed cylinders with a diameter of 9.53 mm and a 1 mm gap between the center cylinder and each out the outer cylinders. The 1 mm gap was to allow for thermal expansion of the susceptors as high temperatures were reached. The susceptors retained a height of 10 mm and a 1 mm thick metal baseplate from the original single cube HX design. This design was proposed as it was already in the process of being made into a physical prototype model, and computational tests were requested to aid in the testing.

Development of the five-cylinder model began with a single cylinder model on a circular

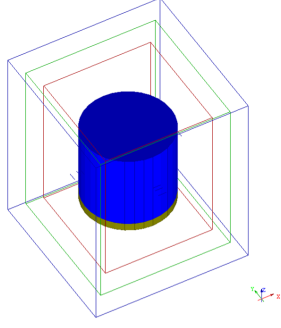


Figure 3.7: Basic cylindrical FDTD model.

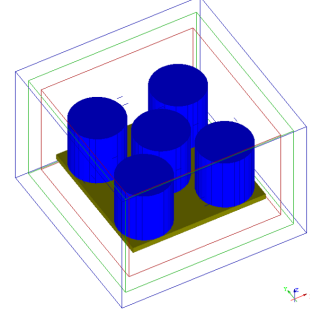


Figure 3.8: Five-cylinder FDTD model.

baseplate. A 32 sector polygon was used to approximate a cylinder. A radius of 5.64 mm was used to give the circular face of the cylinder the same approximate area as the  $10 \times 10$  mm face of the cube. The FDTD model of the single-cylinder susceptor is shown in Figure 3.7. Following the development and testing of this model, a five-cylinder model was developed using the design in Figure 3.5.

Each FDTD model developed is situated inside three boxes: a plane wave box, a “near-to-far” (NTF) box, and an absorbing boundary conditions (ABC) box. The plane wave box is the innermost box and produces the incident plane wave. One face of the plane wave box is selected as the plane wave port, and becomes the source of the plane wave. The NTF box sits just outside the plane wave box, is in charge of near-to-far transformation and is necessary in the project if we want to calculate the scattering patterns of scattering objects irradiated by a plane wave [18]. Finally, the ABC box is the outermost box and imitates the MUR with superabsorption boundary conditions [18]. These boxes are visible in the models shown in Figures 3.7 and 3.8.

With propagation of the plane wave in the negative direction of the  $z$ -axis, the design MMW HX in Figure 3.8 is characterized by the ratio of the absorbing ceramic surface to the reflecting surface of the square metal plate being  $d = 0.598$ , and this implies that this layout may be responsible for lower energy efficiency (compared to a single square susceptor [12,13] with  $d = 1$ ). The solution of the problem on the packing of equal circles in a square [19–21] provides the highest value of  $d$  (0.785) for four, nine, and sixteen cylinders arranged in rigorous rows and columns. This suggests feasibility of studying the layouts of the cylindrical susceptors with four, nine, and sixteen cylinders as possible alternative designs of the MMW HX.

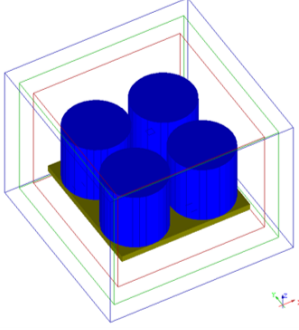


Figure 3.9: Four-cylinder FDTD model.

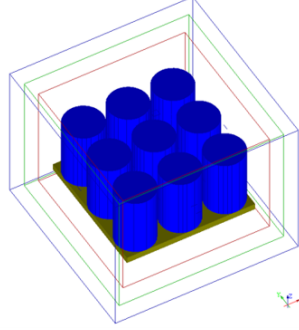


Figure 3.10: Nine-cylinder FDTD model.

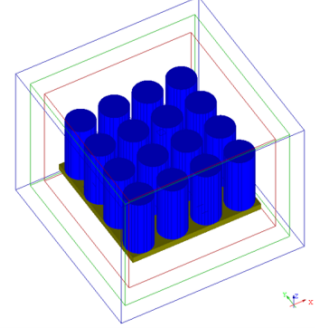


Figure 3.11: Sixteen-cylinder FDTD model.

Three additional models reproducing these three configurations (but for the same size baseplate with length  $L = 24.4$  mm as in the five-cylinder model) were developed (Figures 3.9, 3.10, and 3.11), and employed for the comparative computational analysis.

The single cylinder FDTD model shown in Figure 3.7 is comprised of a single AlN:Mo cylinder of radius 5.64 mm and height 10 mm, on top of a circular baseplate also of radius 5.64 mm and thickness 1 mm. The mesh of the 12.3 mm wide by 12.3 mm long by 10.5 mm tall box surrounding the susceptors has a maximum cell size of 0.095 mm, while the mesh in the air outside the region of the susceptors has a maximum cell size of 0.295 mm. The plane wave box is  $14 \times 14 \times 18$  mm, the NTF box is  $17 \times 17 \times 21$  mm, and the ABC box is  $20 \times 20 \times 24$  mm. The model comprises of 4 304 178 cells, or 410 MB RAM. The UDO script for this design to generate the FDTD model in *QuickWave* are represented in Appendix A.

The four-, five-, nine-, and sixteen-cylinder FDTD models shown in Figures 3.8-3.11 are all comprised of arrays of cylinders of radii 5.86, 4.77, 3.73, and 2.68 mm respectively and height 10 mm. The baseplate in each of these models is  $24.4 \times 24.4$  mm across and 1 mm thick. The meshes of the 25.4 mm wide by 25.4 mm long by 10.5 mm tall box surrounding the susceptors has a maximum cell size of 0.095 mm, while the mesh in the air outside the region of the susceptors has a maximum cell size of 0.295 mm. The plane wave boxes are  $27.4 \times 27.4 \times 18$  mm, the NTF boxes are  $30.4 \times 30.4 \times 21$  mm, and the ABC boxes are  $33.4 \times 33.4 \times 24$  mm. The models comprises of 15 070 050 cells, or 1 437 MB RAM. The UDO scripts for each of these designs to generate the FDTD models in *QuickWave* can also be found in Appendix A.



## 4 Computation of Energy Efficiency

To characterize energy efficiency of the MMW HX, following [13, 14], we calculate the parameter  $\nu = P_d/P$ , where  $P_d$  is density of the EM power dissipated in the composite susceptors and  $P$  is the power density of the incident plane wave. Values of  $P_d$  are computed by the *QuickWave* EM model for different concentrations of Mo in the ceramic composite and its temperatures, and temperature is introduced in EM simulation through complex permittivity  $\varepsilon = \varepsilon' - i\varepsilon''$  (with dielectric constants  $\varepsilon'$  and the loss factor  $\varepsilon''$ ) at particular temperatures. As for power densities,  $P_d$  and  $P$  relate to the total area of the absorbing surfaces of the cylindrical susceptors and the area of the square metal plate carrying all the cylinders, respectively. As such, in the case of a normal incidence, the absorbing surface consists of the circular areas on the top of the cylinders.

### 4.1 Energy Efficiency of Multi-Cylinder Systems

Simulations were run to test and compare the energy efficiencies of the different multi-cylinder models. For all the models tested, simulations were run on all six concentrations of Mo and for six temperature increments: 20 °C, 200 °C, 400 °C, 600 °C, 800 °C, and 1 000 °C.

Simulation of EM processes in the five-cylinder system displays the highest energy efficiency when the cylinders are made of the composite with 3.0-4.0% Mo (Figure 4.1). This is consistent with the results for the system with a single rectangular block [13] (red dots in Figure 4.1), though here the efficiency is down from 54 to 37%. This drop is likely explained by the decrease of the surface area of the absorbing susceptors. The graphs of average energy efficiency for the four- and nine-cylinder systems (Figures 4.2, 4.3) have maxima at slightly higher levels (39 and 43%, respectively), also at 3.0-4.0% Mo. It can be seen that all of the maximums for energy efficiency of

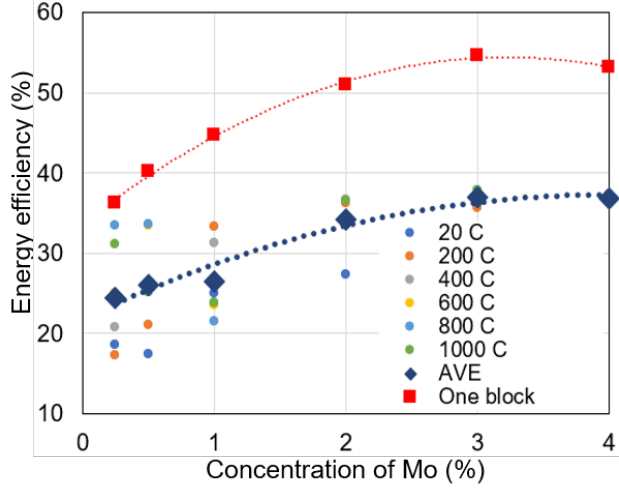


Figure 4.1: Energy efficiency (at different temperatures of the AlN:Mo composite and average) of the experimental five-cylinder system; normal incidence ( $\theta = 0$ ); red points characterize the system with one rectangular AlN:Mo block.

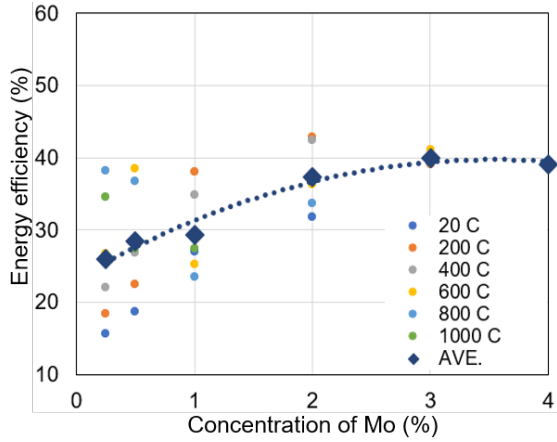


Figure 4.2: Energy efficiency (at different temperatures of the AlN:Mo composite and average) of the experimental four-cylinder system; normal incidence ( $\theta = 0$ ).

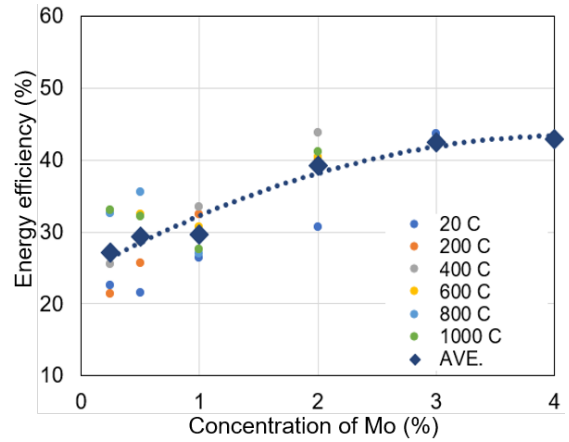


Figure 4.3: Energy efficiency (at different temperatures of the AlN:Mo composite and average) of the experimental nine-cylinder system; normal incidence ( $\theta = 0$ ).

the multi-cylinder models are less than the maximum energy efficiency of the single cube model in all systems considered, which may be a necessary trade off for the mechanical robustness and cost effectiveness of the cylindrical susceptors in comparison the the cubic susceptors.

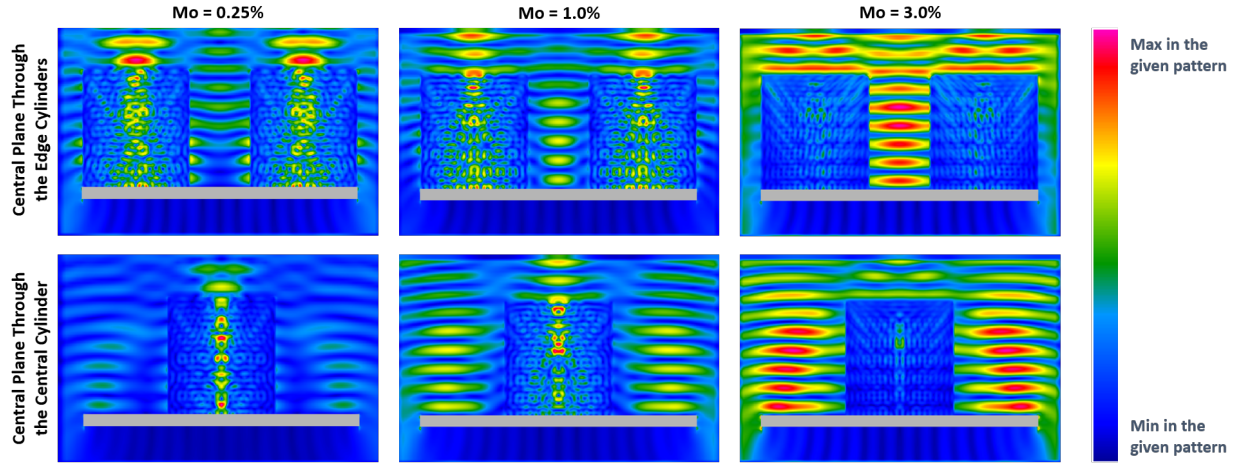


Figure 4.4: Relative patterns of the electric field envelopes in the vertical ( $xz$ -) planes through the five-cylinder system for different concentrations of Mo in the composite susceptors.

## 4.2 Electromagnetic Fields of the Five-Cylinder Model

Computational evaluation of energy efficiency was also supplemented by computation of the electric field. Typical examples of the field envelopes for the susceptors of different contents of doping are shown in Figure 4.4. Growth of Mo concentration from 0.25 to 4% corresponds to the 1.5 times increase of dielectric constant and the drastic (nearly 30 times) jump up of the loss factor (see Table 1.1). Field penetration in the composite with higher contents of Mo is therefore much lower, and the patterns induced show that the magnitude of the electric field in air between and around the cylinders is much higher in case of  $Mo = 3\%$  than of  $Mo = 0.25\%$ . Also, for different Mo contents, there is a different level of reflection from the metal plate on the bottom of the cylinders (and thus a different level of absorption by the lossy susceptors). Combination of all these factors, as seen in Figures 4.1-4.4, makes the composites with a particular concentration of Mo preferential (in terms of energy efficiency) for MMW HX of a particular design.

# 5 Computation of Temperature Fields

## 5.1 Five-Cylinder Systems: Heating Rates

Simulation of the temperature field induced in the ceramic susceptors by the incident plane MMW shows (i) the heating rates, and (ii) volumetric temperature distributions within the ceramic susceptors at different time instances. It is seen from Figure 5.1 that when the plane wave with incoming power density of  $357 \text{ W/mm}^2$  hits the five-cylinder system, then, in the composite with the lowest content of Mo (0.25%), the temperature of  $1000 \text{ }^\circ\text{C}$  is reached after about 90 s; however, in the system made of AlN:Mo with Mo = 4.0%, this level is reached after about 50 s. This can be explained by the fact that the lower the concentration, the lower the loss factor of the composite. For every concentration, the time characteristics of minimum and maximum temperatures are very close to each other, though at higher temperatures the curves are generally further apart for the composites with higher concentrations. This also makes sense: with higher heating rates, the hot spots are heated faster because the loss factor is increasing as a function of temperature.

## 5.2 Multi-Cylinder Models: Temperature Patterns

The last observation suggests that the temperature distributions within ceramic composites should be highly uniform, and this is confirmed by the series of patterns in Figures 5.2-5.4 and Appendix B showing time evolution of temperature field in the cylindrical susceptors. The patterns are indeed remarkably uniform for all concentrations. (This, in turn, justifies the assumption about uniformity of heating that was implicitly used in computations of energy efficiency at different temperatures (Figures 4.1-4.3) by the EM model. There, the temperatures were represented by corresponding values of dielectric constant and the loss factor.)

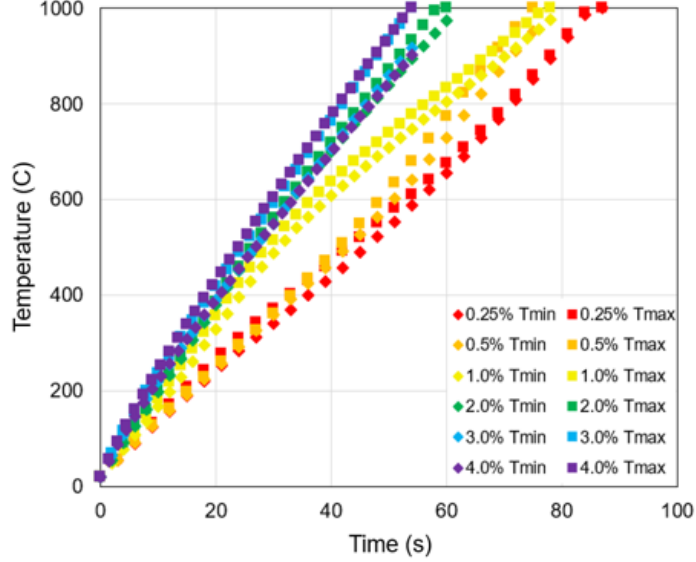


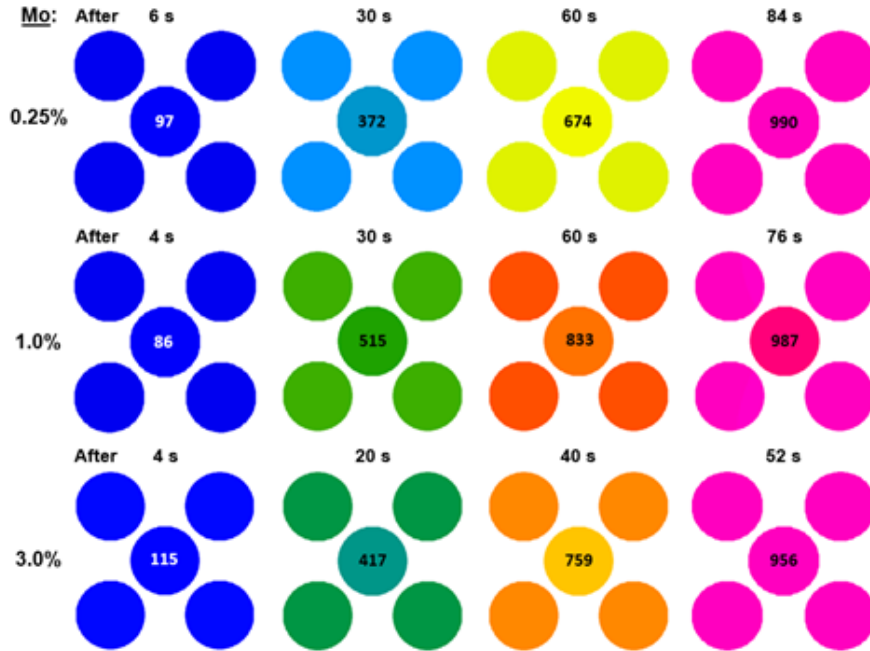
Figure 5.1: Maximum and minimum temperatures throughout the five-cylinder system.

High level of uniformity is kept up to the final stage of heating for each individual cylinder and is maintained in all five cylinders (Figure 5.2). The chief cause for this uncharacteristically homogeneous temperature distribution generated by EM heating is very high level of thermal conductivity of AlN (Figure 1.4) that is barely changed with the incremental Mo doping [26]. It is shown in [13] that in a MMW HX based on a single AlN:Mo block, dissipated power density patterns characterized by dozens of strong hot spots (similar to the patterns in Figures 3.1 and 3.2) are converted into highly uniform temperature patterns maintaining their uniformity for the entire times of the heating process. We observe a similar phenomenon here in the design based on separately standing cylindrical susceptors.

Computation of temperature patterns in the four-cylinder system model (characterized by higher ratio  $d = 0.722$ ) shows a very similar heating process, but even more consistent temperature distributions: all four cylinders are heated at about the same rate with very similar cross-sectional patterns (Figure 5.3). Simulating the heating in the system with higher numbers of cylinders (such as the nine-cylinder system) (Figure 5.4), we see that the central cylinder is heated slower and at the final stage of heating its maximum temperature could be lower by 40-60 °C. On the other hand, the four-cylinder system takes the longest to reach 1000 °C; yet, the delay is only 10 s in comparison with the nine-cylinder system, which is the fastest.



(a)



(b)

Figure 5.2: Time evolution of the temperature field in the vertical ( $xz$ -) plane through the two edge susceptors (a) and in the central horizontal ( $xy$ -) plane through the all susceptors (b) with  $Mo = 0.25, \dots, 4.0\%$  in the five-cylinder model.

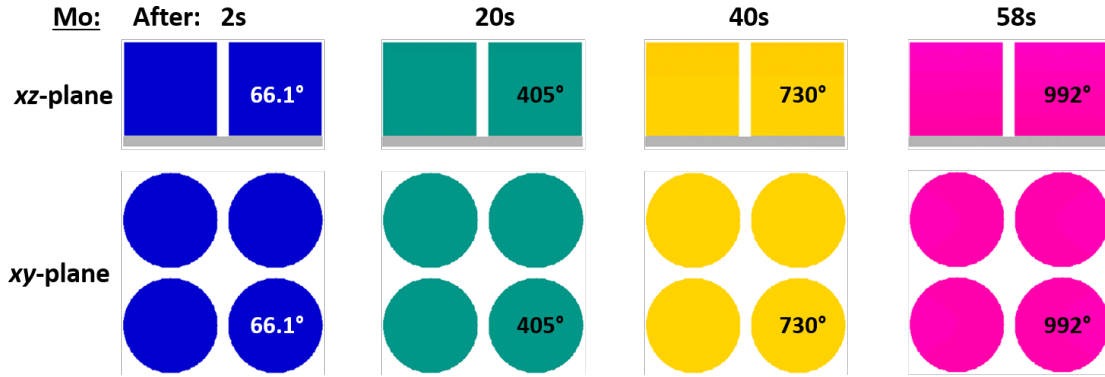


Figure 5.3: Time evolution of the temperature field in the vertical ( $xz$ -) plane through the two edge susceptors and in the central horizontal ( $xy$ -) plane through the all susceptors with  $Mo = 3.0\%$  in the four-cylinder model.

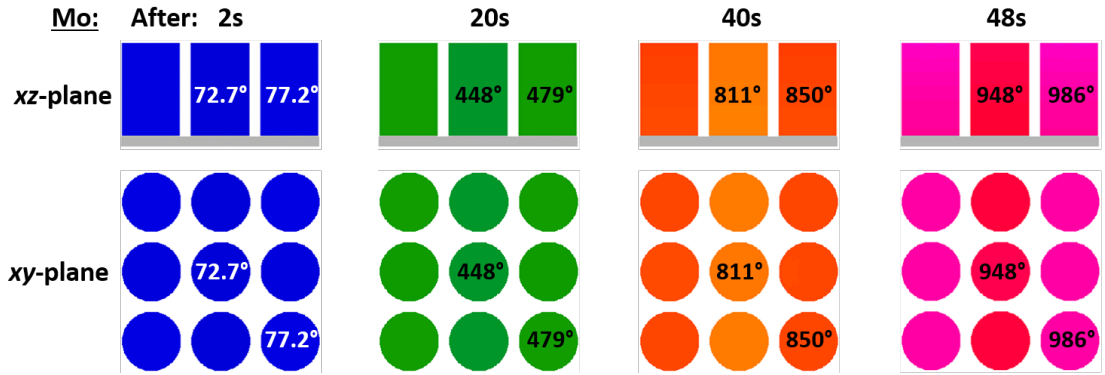


Figure 5.4: Time evolution of the temperature field in the vertical ( $xz$ -) plane through the two edge susceptors and in the central horizontal ( $xy$ -) plane through the all susceptors with  $Mo = 3.0\%$  in the nine-cylinder model.

In all considered systems, temperature distribution along the vertical  $z$ -axis is very uniform. This confirms that using multiple separately standing susceptors does not have a negative impact on uniformity of heating of the metal baseplate.

## 6 Supplementary Topics

### 6.1 Susceptors with a Dielectric Topping

Based on the designs of the walls of anechoic chambers, which are built to eliminate reflections from boundaries of closed spaces, an additional model was created to test the impact of adding a pointed top to the single cylinder model, which otherwise has a flat top surface. Figure 6.1 shows the FDTD model of an AlN:Mo cylinder with the same dimensions as the original single cylinder model (radius 5 mm, height 10 mm) with the addition of a cone of adjustable height on the top face.

The energy efficiency of a single AlN:Mo cylinder with an AlN:Mo cone, also made of AlN:Mo, on top was tested using this model. Figure 6.2 shows the results of these tests, with the  $x$ -axis representing the height of the pointed top (ranging from 0 mm to 12 mm), the  $y$ -axis representing energy efficiency defined, following Section 4, as the ratio of absorbed power to incoming power; the different curves in the figure represent the different concentrations of Mo in the AlN:Mo. Energy efficiency for the cylinder and cone with 3.0% Mo showed the highest energy efficiency, remaining a consistent 60% for each height of the cone that was tested, including 0 mm (Figure 6.2). This suggests that, in the case of an AlN:Mo cone, energy efficiency is not impacted by the use of a cone atop the cylinder. The developed model can be used in future computational tests of the effect made on the performance of the MMW HX by cones made from other applicable materials.



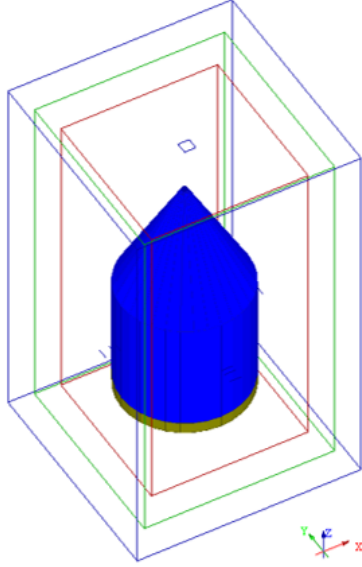


Figure 6.1: Model of a single cylinder with pointed top.

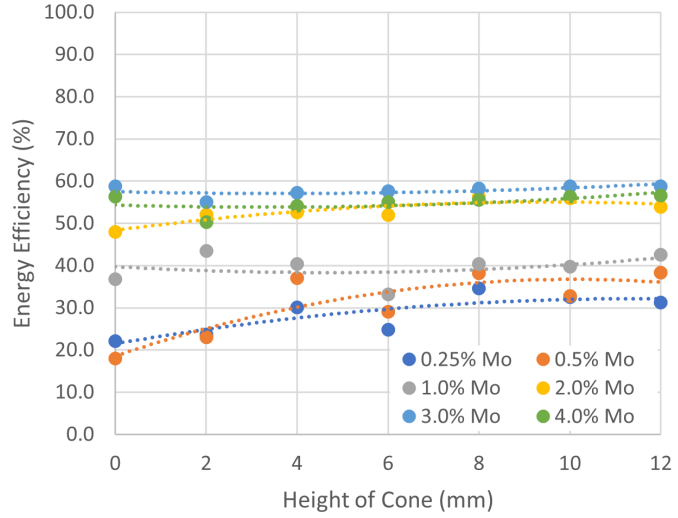


Figure 6.2: Energy efficiency of the single-cylinder system with an AlN:Mo cone on the top surface at different heights of the cone; normal incidence ( $\theta = 0$ ).

## 6.2 Off-Normal Incidence

To properly understand and compare the energy efficiency of the various models, the absorbed power is given as a ratio of the overall power absorbed by the susceptors divided by the exposed surface area of the susceptors. This is simple calculation when the angle of incidence  $\theta$  is  $0^\circ$  (Figure 3.6), as the exposed surface area is just the top face of the susceptors (squares in the case of the cubic models, and circles in the case of the cylindrical models). However, the calculation of exposed surface area becomes more complex. When the plane wave has off-normal incidence, such as in Figure 6.3, the calculations for exposed surface area must also include the regions of the sides of the cylinders now visible while also accounting for any areas that overlap. The derivation of a formula for this area is outlined in Appendix C, and a MATLAB script for the final calculation is recorded in Appendix D. This was done to support future computational study of the effect of off-normal incidence.

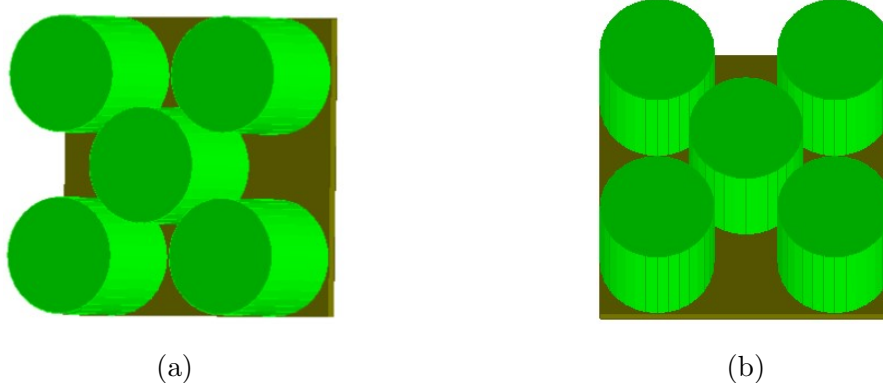


Figure 6.3: Five-cylinder FDTD model with off-normal plane wave incidence with inclination along the  $x$ -axis (a) and  $y$ -axis (b)

### 6.3 Thermal Boundary Conditions

To determine the impact of the heat transfer coefficient  $h$  on the adequacy of the FDTD models of the millimeter-wave absorber, two thermal boundary condition (BC) cases in the thermal problem must be considered. The direct testing of the developed models at 95 GHz frequency is not possible due to the computational resources required to run the simulation, but a comparison can be done at a lower frequency (e.g., at 2.45 GHz). Because the EM and thermal properties of AlN:Mo at 2.45 GHz are not known, the comparison was instead done using a cube with EM and thermal material parameters of zirconia taken from [30]. A larger cube (e.g., 100 mm on each side) was used to better match the wavelength to cube size ratio of the original 95 GHz problem.

The overall impact of the convective heat transfer coefficient  $h$  on BCs is dependant on the type of BCs implemented. In explicit, or Dirichlet, BCs, the temperature  $T_B$  at the boundary is explicitly defined and kept constant at the temperature  $T_S$  of the air surrounding the susceptor, as in (1). In adiabatic, or Neumann, BCs, the boundary experiences zero heat flow without a specific temperature being defined, as (2). In between these two extremes are convective (or Robin) BCs, which are dependant on both  $h$  and  $T_S$ , as in (3).

$$T_B = T_S \quad (1)$$

$$\frac{dT_B}{dn} = 0 \quad (2)$$

$$\frac{dT_B}{dn} = h(T_B - T_S) \quad (3)$$

The  $h$  coefficient describes how the heat is transferred between the surface of the object and the environment. The convective BC with  $h$  coefficient set to 0 becomes adiabatic BC, while  $h$  value tending to infinity makes it behave like the explicit BC [18].

Initial computational tests were carried out in this project as a preliminary step in a computational study of an impact of the value of  $h$  in thermal BC on the temperature field in the MMW HX simulated with the coupled EM-thermal *QuickWave* models. In the first test, all six faces of the zirconia cube have adiabatic BCs, imitating full thermal isolation. In the second test, all six faces of the zirconia cube have explicit BCs, where the boundaries are held at a constant 25 °C. These two cases are the extreme scenarios for boundary conditions, but in real-world situations a convective BC with non-zero  $h$  are expected to be used. For both extreme cases, the simulations run until the ceramic cube reaches a maximum temperature of 324 °C, which is the highest temperature with known properties for the zirconia cube and at 2.45 GHz. Preliminary results of the tests on the zirconia cube show little difference in the temperature patterns of the two tests with 1 and 2, indicating that the impact of boundary conditions on the overall model is low. Details of these tests can be found in Appendix E.

For the values of  $h$  between the two extremes, its approximate value can be used in *QuickWave* as an input parameter for the model, allowing convective BCs to be applied. The convective heat transfer coefficient can be estimated using physical data of AlN:Mo. A particular approach leading to the approximate value of  $h$  for the air-composite interface is outlined in Appendix F.

## 7 Conclusion

The present MQP was focused on multiphysics modeling of electromagnetic and thermal processes in millimeter-wave heat exchanger with multiple cylindrical susceptors made of AlN:Mo ceramic composite. Aluminum nitride with 3.0-4.0% Mo by volume provided the highest energy efficiencies and most uniform temperature patterns for all layouts of the cylindrical susceptors. These results are consistent with the output of the earlier modeling projects done on the system with a single cubic susceptor. The most noticeable difference is that here the energy efficiency is lower.

The models with four, nine, and sixteen cylinders were selected for computational tests due to their high densities in the circles in a square packing problem, yet the energy efficiency of the tested systems is about the same as in the five-cylinder layout.

Simulation of the temperature field induced in the composite by the incident field shows that distribution of temperature both in the horizontal cross-section and along the vertical axis is highly uniform in all systems. Therefore, given the rationale for the cylindrical shapes of the ceramic susceptors, they all can be recommended for implementation in practical MMW HXs.

The results of this MQP are ready to be taken into consideration by the project sponsor, the Air Force Research Laboratory, when preparing the experimental phase of the project. At the same time, this MQP made initial steps in some related topics important for further development of this technology: the impact of thermal boundary condition on the temperature distribution in the output of the models, the impact of the angle of incidence on the energy efficiency of the systems, and the practicality of pointed cones on the susceptors to decrease the level of reflection of the EM field. With our preliminary work, all of these topics can be explored in depth in future computational studies.

# Appendices

## A UDO Scripts for *QuickWave* Models with Cylindrical Susceptors

Within the *QuickWave* software, models can be generated by writing a script using the User Defined Object (UDO) language. In a UDO script, the user starts by defining all of the necessary parameters for the model being created. Once the parameters are defined, they are used in various “CALL” functions to generate the different elements of the model being created. For the models of the MMW HXs with cylindrical susceptors, five different call functions are used:

- CYV: a vertical cylinder defined by the radius, the height, the number of polygonic sectors, the medium, and the  $x$ ,  $y$ , and  $z$  coordinates.
- CUBO: a cube-shaped baseplate defined by the  $x$ ,  $y$ , and  $z$  dimensions, the medium, and the  $x$ ,  $y$ , and  $z$  coordinates.
- NTF: the NTF and ABC boxes defined by their respective  $x$ ,  $y$ , and  $z$  dimensions, various BC properties, and the  $x$ ,  $y$ , and  $z$  coordinates.
- PLW\_PURE: a plane-wave box defined by the  $x$ ,  $y$ , and  $z$  dimensions, the medium, and the  $x$ ,  $y$ , and  $z$  coordinates.
- SP: special planes are used to control the FDTD mesh by specifying boundaries between the layers of cells; here they are used to mark a boundary of a susceptor, the baseplate, the air, and the plane wave box, or to define the size of the FDTD cells; defined by the type of plane being used, the combination of  $x$ ,  $y$ , and  $z$  directions making up the plane, the  $x$ ,  $y$ , and  $z$  coordinates, and (if the SP is defining FDTD mesh) the cell size of the mesh being defined.

The UDO scripts for the MMW HX models with cylindrical susceptors, pictured in Figures 3.7-3.11, are listed below.

## UDO Script for Single Cylinder Model

```
comment="AlN:Mo cylinder inside a plane wave box surrounded by NTF+ABC
boxes - vertical model";
bitmap="AlNMoM.jpg";

PAR( "Abs length (x-dir)", d, 20 );
PAR( "Abs width (y-dir)", s, 20 );
PAR( "Abs height (z-dir)", w, 24 );
PAR( "NTFLength (x-dir)", dntf, 17 );
PAR( "NTFWidth (y-dir)", sntf, 17 );
PAR( "NTFHeight (z-dir)", wntf, 21 );
PAR( "Plane wave box length (x-dir)", pld, 14 );
PAR( "Plane wave box width (y-dir)", pls, 14 );
PAR( "Plane wave box height (z-dir)", plw, 18 );
PAR( "Plane wave port file name", plp, plw1 );
PAR( "AlN:Mo cylinder: radius", cr, 5.642 );
PAR( "AlN:Mo cylinder: thickness (z-dir)", ch, 10 );
PAR( "AlN:Mo cylinder: number of sectors", cn, 32 );
PAR( "AlN:Mo cylinder: medium", cmed, AlN );
PAR( "Metal plate: radius", mr, 5.642 );
PAR( "Metal plate: thickness (z-dir)", mh, 1 );
PAR( "Metal plate: number of sectors", mn, 32 );
PAR( "Metal plate: medium", mmed, metal );
PAR( "Cell size in air", cair, 0.295 );
PAR( "Cell size in AlN:Mo block", ccer, 0.095 );

ENDHEADER;

OPENOBJECT( plwntf3 );

MESHPAR ( cair, cair, cair, 1, 2, 1, 2, 1, 2, 1 );

dh = 0.5*d;
sh = 0.5*s;
wh = 0.5*w;

# AlN:Mo cylinder
CALL( "elements/cyv.udo", cylobj1, cr, ch, cn, cmed, N, x, y, z-ch/2,
```

```

10 );

# Adjacent metal plate
CALL( "elements/cyv.udo", plateobj, mr, mh, mn, mmed, E, x, y,
      z-ch/2-mh, 10 );

# NTF and ABC boxes
CALL( "boxes/ntf.udo", d, s, w, dntf, sntf, wntf, N, N, N, x-dh, y-sh,
      z-wh, 13 );

# Plane wave surfaces
CALL( "boxes/plw_pure.udo", plwbox, pld, pls, plw, plp, x, y, z, 9 );

# SPs
CALL( "elements/specxu.udo", spxu1, 1, ccer, x-cr-0.5, y, z, 7 );
CALL( "elements/specxd.udo", spxd1, 1, ccer, x+cr+0.5, y, z, 7 );
CALL( "elements/specyu.udo", spyu1, 1, ccer, x, y-cr-0.5, z, 7 );
CALL( "elements/specyd.udo", spyd1, 1, ccer, x, y+cr+0.5, z, 7 );
CALL( "elements/speczu.udo", spzu1, 1, ccer, x, y, z-ch/2, 7 );
CALL( "elements/speczd.udo", spzd1, 1, ccer, x, y, z+ch/2+0.5, 7 );
CALL( "elements/specx.udo", spxu1, 1, x-cr, y, z, 6 );
CALL( "elements/specx.udo", spxd1, 1, x+cr, y, z, 6 );
CALL( "elements/specy.udo", spyu1, 1, x, y-cr, z, 6 );
CALL( "elements/specy.udo", spyd1, 1, x, y+cr, z, 6 );
CALL( "elements/specz.udo", spzu1, 1, x, y, z-ch/2, 6 );
CALL( "elements/specz.udo", spzd1, 1, x, y, z+ch/2, 6 );
CALL( "elements/specx.udo", spx1, 1, x-pld/2, y, z, 6 );
CALL( "elements/specx.udo", spx2, 1, x+pld/2, y, z, 6 );
CALL( "elements/specy.udo", spy1, 1, x, y-pls/2, z, 6 );
CALL( "elements/specy.udo", spy2, 1, x, y+pls/2, z, 6 );
CALL( "elements/specz.udo", spz1, 1, x, y, z-plw/2, 6 );
CALL( "elements/specz.udo", spz2, 1, x, y, z+plw/2, 6 );
CALL( "elements/specz.udo", spx3, 1, x, y, z-ch/2-mh, 6 );

CLOSEOBJ;

```

## UDO Script for Four-Cylinder Model

```
comment="4 AlN:Mo cylinders with set plate dimensions inside a plane
      wave box surrounded by NTF+ABC boxes";
bitmap="AlNMoM.jpg";

PAR( "Plane wave port file name", plp, plw1 );
PAR( "AlN:Mo cylinder: thickness (z-dir)", ch, 10 );
PAR( "AlN:Mo cylinder: number of sectors", cn, 32 );
PAR( "AlN:Mo cylinder: medium", cmed, AlN );
PAR( "Spacing between cylinders", spc, 1 );
PAR( "Metal plate: length (x- and y-dir)", mdx, 21 );
PAR( "Metal plate: thickness (z-dir)", mdz, 1 );
PAR( "Metal plate: medium", mmed, metal );
PAR( "Cell size in air", cair, 0.295 );
PAR( "Cell size in AlN:Mo cylinder", ccer, 0.095 );

ENDHEADER;

OPENOBJECT( plwntf3 );

MESHPAR ( cair, cair, cair, 1, 2, 1, 2, 1, 2, 1 );

cr = (mdx-spc)/4;
a = cr+0.5*spc;

# AlN:Mo cylinders
CALL( "elements/cyv.udo", cylobj1, cr, ch, cn, cmed, N, x-a, y+a,
      z-ch/2, 10 );
CALL( "elements/cyv.udo", cylobj2, cr, ch, cn, cmed, N, x+a, y+a,
      z-ch/2, 10 );
CALL( "elements/cyv.udo", cylobj3, cr, ch, cn, cmed, N, x-a, y-a,
      z-ch/2, 10 );
CALL( "elements/cyv.udo", cylobj4, cr, ch, cn, cmed, N, x+a, y-a,
      z-ch/2, 10 );

# Adjacent metal plate
CALL( "basic/cubo.udo", plateobj, mdx, mdx, mdz, mmed, E, 0, x, y,
      z-ch/2-mdz, 11 );
```



```

# NTF and ABC boxes
d = mdx+9;
s = mdx+9;
w = 24;

dh = 0.5*d;
sh = 0.5*s;
wh = 0.5*w;

dntf = mdx+6;
sntf = mdx+6;
wntf = 21;

CALL( "boxes/ntf.udo", d, s, w, dntf, sntf, wntf, N, N, N, x-dh, y-sh,
      z-wh, 13 );

# Plane wave surfaces
pld = mdx+3;
pls = mdx+3;
plw = 18;

CALL( "boxes/plw_pure.udo", plwbox, pld, pls, plw, plp, x, y, z, 9 );

# SPs
  # Mesh
CALL( "elements/specxu.udo", spx1, 1, ccer, x-mdx/2-0.5, y, z, 7 );
CALL( "elements/specxd.udo", spx2, 1, ccer, x+mdx/2+0.5, y, z, 7 );
CALL( "elements/specyu.udo", spy1, 1, ccer, x, y-mdx/2-0.5, z, 7 );
CALL( "elements/specyd.udo", spy2, 1, ccer, x, y+mdx/2+0.5, z, 7 );
CALL( "elements/speczu.udo", spz1, 1, ccer, x, y, z-ch/2, 7 );
CALL( "elements/speczd.udo", spz2, 1, ccer, x, y, z+ch/2+0.5, 7 );
CALL( "elements/specx.udo", spx1, 1, x-mdx/2, y, z, 6 );
CALL( "elements/specx.udo", spx2, 1, x+mdx/2, y, z, 6 );
CALL( "elements/specy.udo", spy1, 1, x, y-mdx/2, z, 6 );
CALL( "elements/specy.udo", spy2, 1, x, y+mdx/2, z, 6 );
CALL( "elements/specz.udo", spz1, 1, x, y, z-ch/2, 6 );
CALL( "elements/specz.udo", spz2, 1, x, y, z+ch/2, 6 );
  # Cylinder 1

```

```

CALL( "elements/specx.udo", spc2x, 1, x-(a-cr), y+a, z, 6 );
CALL( "elements/specy.udo", spc2y, 1, x-a, y+(a-cr), z, 6 );
# Cylinder 2
CALL( "elements/specx.udo", spc3x, 1, x+(a-cr), y+a, z, 6 );
CALL( "elements/specy.udo", spc3y, 1, x+a, y+(a-cr), z, 6 );
# Cylinder 3
CALL( "elements/specx.udo", spc4x, 1, x-(a-cr), y-a, z, 6 );
CALL( "elements/specy.udo", spc4y, 1, x-a, y-(a-cr), z, 6 );
# Cylinder 4
CALL( "elements/specx.udo", spc5x, 1, x+(a-cr), y-a, z, 6 );
CALL( "elements/specy.udo", spc5y, 1, x+a, y-(a-cr), z, 6 );
# Top and Bottom of Cylinders
CALL( "elements/specz.udo", spm, 1, x, y, z-ch/2, 6 );
CALL( "elements/specz.udo", spm, 1, x, y, z+ch/2, 6 );
# Bottom of Metal Plate
CALL( "elements/specz.udo", spm, 1, x, y, z-ch/2-mdz, 6 );
# Plane Wave Box
CALL( "elements/specx.udo", spplx1, 1, x-pld/2, y, z, 6 );
CALL( "elements/specx.udo", spplx2, 1, x+pld/2, y, z, 6 );
CALL( "elements/specy.udo", spply1, 1, x, y-pls/2, z, 6 );
CALL( "elements/specy.udo", spply2, 1, x, y+pls/2, z, 6 );
CALL( "elements/specz.udo", spplz1, 1, x, y, z-plw/2, 6 );
CALL( "elements/specz.udo", spplz2, 1, x, y, z+plw/2, 6 );

CLOSEOBJ;

```

## UDO Script for Five-Cylinder Model

```
comment="5 AlN:Mo cylinders inside a plane wave box surrounded by
      NTF+ABC boxes";
bitmap="AlNMoM.jpg";

PAR( "Abs length (x-dir)", d, 34 );
PAR( "Abs width (y-dir)", s, 34 );
PAR( "Abs height (z-dir)", w, 24 );
PAR( "NTFLength (x-dir)", dntf, 31 );
PAR( "NTFWidth (y-dir)", sntf, 31 );
PAR( "NTFHeight (z-dir)", wntf, 21 );
PAR( "Plane wave box length (x-dir)", pld, 28 );
PAR( "Plane wave box width (y-dir)", pls, 28 );
PAR( "Plane wave box height (z-dir)", plw, 18 );
PAR( "Plane wave port file name", plp, plw1 );
PAR( "AlN:Mo cylinder: radius", cr, 4.765 );
PAR( "AlN:Mo cylinder: thickness (z-dir)", ch, 10 );
PAR( "AlN:Mo cylinder: number of sectors", cn, 32 );
PAR( "AlN:Mo cylinder: medium", cmed, AlN );
PAR( "Spacing between cylinders", spc, 1 );
PAR( "Metal plate: thickness (z-dir)", mdz, 1 );
PAR( "Metal plate: medium", mmed, metal );
PAR( "Cell size in air", cair, 0.295 );
PAR( "Cell size in AlN:Mo cylinder", ccer, 0.095 );

ENDHEADER;

OPENOBJECT( plwntf3 );

MESHPAR ( cair, cair, cair, 1, 2, 1, 2, 1, 2, 1 );

dh = 0.5*d;
sh = 0.5*s;
wh = 0.5*w;

# AlN:Mo cylinders
CALL( "elements/cyv.udo", cylobj1, cr, ch, cn, cmed, N, x, y, z-ch/2, 10 );
CALL( "elements/cyv.udo", cylobj2, cr, ch, cn, cmed, N,
```

```

    x-cr/sqrt(2)-cr/sqrt(2)-spc/sqrt(2),
    y+cr/sqrt(2)+cr/sqrt(2)+spc/sqrt(2), z-ch/2, 10 );
CALL( "elements/cyv.udo", cylobj3, cr, ch, cn, cmed, N,
    x+cr/sqrt(2)+cr/sqrt(2)+spc/sqrt(2),
    y+cr/sqrt(2)+cr/sqrt(2)+spc/sqrt(2), z-ch/2, 10 );
CALL( "elements/cyv.udo", cylobj4, cr, ch, cn, cmed, N,
    x-cr/sqrt(2)-cr/sqrt(2)-spc/sqrt(2),
    y-cr/sqrt(2)-cr/sqrt(2)-spc/sqrt(2), z-ch/2, 10 );
CALL( "elements/cyv.udo", cylobj5, cr, ch, cn, cmed, N,
    x+cr/sqrt(2)+cr/sqrt(2)+spc/sqrt(2),
    y-cr/sqrt(2)-cr/sqrt(2)-spc/sqrt(2), z-ch/2, 10 );

# Adjacent metal plate
mdx = cr*sqrt(2)+cr*sqrt(2)+spc*sqrt(2)+cr*2;
mdy = cr*sqrt(2)+cr*sqrt(2)+spc*sqrt(2)+cr*2;
CALL( "basic/cubo.udo", plateobj, mdx, mdy, mdz, mmed, E, 0, x, y,
    z-ch/2-mdz, 11 );

# NTF and ABC boxes
CALL( "boxes/ntf.udo", d, s, w, dntf, sntf, wntf, N, N, N, x-dh, y-sh,
    z-wh, 13 );

# Plane wave surfaces
CALL( "boxes/plw_pure.udo", plwbox, pld, pls, plw, plp, x, y, z, 9 );

# SPs
    # Mesh
CALL( "elements/specxu.udo", spx1, 1, ccer, x-mdx/2-0.5, y, z, 7 );
CALL( "elements/specxd.udo", spx2, 1, ccer, x+mdx/2+0.5, y, z, 7 );
CALL( "elements/specyu.udo", spy1, 1, ccer, x, y-mdy/2-0.5, z, 7 );
CALL( "elements/specyd.udo", spy2, 1, ccer, x, y+mdy/2+0.5, z, 7 );
CALL( "elements/speczu.udo", spz1, 1, ccer, x, y, z-ch/2, 7 );
CALL( "elements/speczd.udo", spz2, 1, ccer, x, y, z+ch/2+0.5, 7 );
CALL( "elements/specx.udo", spx1, 1, x-mdx/2, y, z, 6 );
CALL( "elements/specx.udo", spx2, 1, x+mdx/2, y, z, 6 );
CALL( "elements/specy.udo", spy1, 1, x, y-mdy/2, z, 6 );
CALL( "elements/specy.udo", spy2, 1, x, y+mdy/2, z, 6 );
CALL( "elements/specz.udo", spz1, 1, x, y, z-ch/2, 6 );
CALL( "elements/specz.udo", spz2, 1, x, y, z+ch/2, 6 );

```

```

# Cylinder 1
CALL( "elements/specx.udo", spc1x, 1, x-2*cr/sqrt(2)-spc/sqrt(2)+cr,
      y+2*cr/sqrt(2)+spc/sqrt(2), z, 6 );
CALL( "elements/specy.udo", spc1y, 1, x-2*cr/sqrt(2)-spc/sqrt(2),
      y+2*cr/sqrt(2)+spc/sqrt(2)-cr, z, 6 );
# Cylinder 2
CALL( "elements/specx.udo", spc2x, 1, x+2*cr/sqrt(2)+spc/sqrt(2)-cr,
      y+2*cr/sqrt(2)+spc/sqrt(2), z, 6 );
CALL( "elements/specy.udo", spc2y, 1, x+2*cr/sqrt(2)+spc/sqrt(2),
      y+2*cr/sqrt(2)+spc/sqrt(2)-cr, z, 6 );
# Cylinder 3
CALL( "elements/specx.udo", spc3x1, 1, x-cr, y, z, 6 );
CALL( "elements/specx.udo", spc3x2, 1, x+cr, y, z, 6 );
CALL( "elements/specy.udo", spc3x2, 1, x, y-cr, z, 6 );
CALL( "elements/specy.udo", spc3x2, 1, x, y+cr, z, 6 );
# Cylinder 4
CALL( "elements/specx.udo", spc4x, 1, x-2*cr/sqrt(2)-spc/sqrt(2)+cr,
      y-2*cr/sqrt(2)-spc/sqrt(2), z, 6 );
CALL( "elements/specy.udo", spc4y, 1, x-2*cr/sqrt(2)-spc/sqrt(2),
      y-2*cr/sqrt(2)-spc/sqrt(2)+cr, z, 6 );
# Cylinder 5
CALL( "elements/specx.udo", spc5x, 1, x+2*cr/sqrt(2)+spc/sqrt(2)-cr,
      y-2*cr/sqrt(2)-spc/sqrt(2), z, 6 );
CALL( "elements/specy.udo", spc5y, 1, x+2*cr/sqrt(2)+spc/sqrt(2),
      y-2*cr/sqrt(2)-spc/sqrt(2)+cr, z, 6 );
# Top and Bottom of Cylinders
CALL( "elements/specz.udo", spm, 1, x, y, z-ch/2, 6 );
CALL( "elements/specz.udo", spm, 1, x, y, z+ch/2, 6 );
# Bottom of Metal Plate
CALL( "elements/specz.udo", spm, 1, x, y, z-ch/2-mdz, 6 );
# Plane Wave Box
CALL( "elements/specx.udo", spplx1, 1, x-pld/2, y, z, 6 );
CALL( "elements/specx.udo", spplx2, 1, x+pld/2, y, z, 6 );
CALL( "elements/specy.udo", spply1, 1, x, y-pls/2, z, 6 );
CALL( "elements/specy.udo", spply2, 1, x, y+pls/2, z, 6 );
CALL( "elements/specz.udo", spplz1, 1, x, y, z-plw/2, 6 );
CALL( "elements/specz.udo", spplz2, 1, x, y, z+plw/2, 6 );

CLOSEOBJ;

```

## UDO Script for Nine-Cylinder Model

```
comment="9 AlN:Mo cylinders on a plate with set dimensions inside a  
plane wave box surrounded by NTF+ABC boxes";  
bitmap="AlNMoM.jpg";
```

```
PAR( "Plane wave port file name", plp, plw1 );  
PAR( "AlN:Mo cylinder: thickness (z-dir)", ch, 10 );  
PAR( "AlN:Mo cylinder: number of sectors", cn, 32 );  
PAR( "AlN:Mo cylinder: medium", cmed, AlN );  
PAR( "Spacing between cylinders", spc, 1 );  
PAR( "Metal plate: length (x- and y-dir)", mdx, 21 );  
PAR( "Metal plate: thickness (z-dir)", mdz, 1 );  
PAR( "Metal plate: medium", mmed, metal );  
PAR( "Cell size in air", cair, 0.295 );  
PAR( "Cell size in AlN:Mo cylinder", ccer, 0.095 );
```

```
ENDHEADER;
```

```
OPENOBJECT( plwntf3 );
```

```
MESHPAR ( cair, cair, cair, 1, 2, 1, 2, 1, 2, 1 );
```

```
cr = (mdx-2*spc)/6;
```

```
a = cr+0.5*spc;
```

```
# AlN:Mo cylinders
```

```
CALL( "elements/cyv.udo", cylobj1, cr, ch, cn, cmed, N, x-2*a, y+2*a,  
z-ch/2, 10 );
```

```
CALL( "elements/cyv.udo", cylobj2, cr, ch, cn, cmed, N, x, y+2*a,  
z-ch/2, 10 );
```

```
CALL( "elements/cyv.udo", cylobj3, cr, ch, cn, cmed, N, x+2*a, y+2*a,  
z-ch/2, 10 );
```

```
CALL( "elements/cyv.udo", cylobj4, cr, ch, cn, cmed, N, x-2*a, y,  
z-ch/2, 10 );
```

```
CALL( "elements/cyv.udo", cylobj5, cr, ch, cn, cmed, N, x, y, z-ch/2,  
10 );
```

```
CALL( "elements/cyv.udo", cylobj6, cr, ch, cn, cmed, N, x+2*a, y,  
z-ch/2, 10 );
```

```

CALL( "elements/cyv.udo", cylobj7, cr, ch, cn, cmed, N, x-2*a, y-2*a,
      z-ch/2, 10 );
CALL( "elements/cyv.udo", cylobj8, cr, ch, cn, cmed, N, x, y-2*a,
      z-ch/2, 10 );
CALL( "elements/cyv.udo", cylobj9, cr, ch, cn, cmed, N, x+2*a, y-2*a,
      z-ch/2, 10 );

# Adjacent metal plate
CALL( "basic/cubo.udo", plateobj, mdx, mdx, mdz, mmed, E, 0, x, y,
      z-ch/2-mdz, 11 );

# NTF and ABC boxes
d = mdx+9;
s = mdx+9;
w = 24;

dh = 0.5*d;
sh = 0.5*s;
wh = 0.5*w;

dntf = mdx+6;
sntf = mdx+6;
wntf = 21;

CALL( "boxes/ntf.udo", d, s, w, dntf, sntf, wntf, N, N, N, x-dh, y-sh,
      z-wh, 13 );

# Plane wave surfaces
pld = mdx+3;
pls = mdx+3;
plw = 18;

CALL( "boxes/plw_pure.udo", plwbox, pld, pls, plw, plp, x, y, z, 9 );

# SPs
# Mesh
CALL( "elements/specxu.udo", spx1, 1, ccer, x-mdx/2-0.5, y, z, 7 );
CALL( "elements/specxd.udo", spx2, 1, ccer, x+mdx/2+0.5, y, z, 7 );
CALL( "elements/specyu.udo", spy1, 1, ccer, x, y-mdx/2-0.5, z, 7 );

```

```

CALL( "elements/specyd.udo", spy2, 1, ccer, x, y+mdx/2+0.5, z, 7 );
CALL( "elements/speczu.udo", spz1, 1, ccer, x, y, z-ch/2, 7 );
CALL( "elements/speczd.udo", spz2, 1, ccer, x, y, z+ch/2+0.5, 7 );
CALL( "elements/specx.udo", spx1, 1, x-mdx/2, y, z, 6 );
CALL( "elements/specx.udo", spx2, 1, x+mdx/2, y, z, 6 );
CALL( "elements/specy.udo", spy1, 1, x, y-mdx/2, z, 6 );
CALL( "elements/specy.udo", spy2, 1, x, y+mdx/2, z, 6 );
CALL( "elements/specz.udo", spz1, 1, x, y, z-ch/2, 6 );
CALL( "elements/specz.udo", spz2, 1, x, y, z+ch/2, 6 );
    # Cylinder 1
CALL( "elements/specx.udo", spc1x, 1, x-(spc+cr), y+2*a, z, 6 );
CALL( "elements/specy.udo", spc1y, 1, x-2*a, y+(spc+cr), z, 6 );
    # Cylinder 2
CALL( "elements/specx.udo", spc2x1, 1, x-cr, y+2*a, z, 6 );
CALL( "elements/specx.udo", spc2x2, 1, x+cr, y+2*a, z, 6 );
CALL( "elements/specy.udo", spc2y, 1, x, y+(spc+cr), z, 6 );
    # Cylinder 3
CALL( "elements/specx.udo", spc3x, 1, x+(spc+cr), y+2*a, z, 6 );
CALL( "elements/specy.udo", spc3y, 1, x+2*a, y+(spc+cr), z, 6 );
    # Cylinder 4
CALL( "elements/specx.udo", spc4x, 1, x-(spc+cr), y, z, 6 );
CALL( "elements/specy.udo", spc4y1, 1, x-2*a, y+cr, z, 6 );
CALL( "elements/specy.udo", spc4y2, 1, x-2*a, y-cr, z, 6 );
    # Cylinder 5
CALL( "elements/specx.udo", spc5x1, 1, x-cr, y, z, 6 );
CALL( "elements/specx.udo", spc5x2, 1, x+cr, y, z, 6 );
CALL( "elements/specy.udo", spc5y1, 1, x, y-cr, z, 6 );
CALL( "elements/specy.udo", spc5y2, 1, x, y+cr, z, 6 );
    # Cylinder 6
CALL( "elements/specx.udo", spc6x, 1, x+(spc+cr), y, z, 6 );
CALL( "elements/specy.udo", spc6y1, 1, x+2*a, y+cr, z, 6 );
CALL( "elements/specy.udo", spc6y2, 1, x+2*a, y-cr, z, 6 );
    # Cylinder 7
CALL( "elements/specx.udo", spc7x, 1, x-(spc+cr), y-2*a, z, 6 );
CALL( "elements/specy.udo", spc7y, 1, x-2*a, y-(spc+cr), z, 6 );
    # Cylinder 8
CALL( "elements/specx.udo", spc8x1, 1, x-cr, y-2*a, z, 6 );
CALL( "elements/specx.udo", spc8x2, 1, x+cr, y-2*a, z, 6 );
CALL( "elements/specy.udo", spc2y, 1, x, y-(spc+cr), z, 6 );

```



```

# Cylinder 9
CALL( "elements/specx.udo", spc9x, 1, x+(spc+cr), y-2*a, z, 6 );
CALL( "elements/specy.udo", spc9y, 1, x+2*a, y-(spc+cr), z, 6 );
# Top and Bottom of Cylinders
CALL( "elements/specz.udo", spm, 1, x, y, z-ch/2, 6 );
CALL( "elements/specz.udo", spm, 1, x, y, z+ch/2, 6 );
# Bottom of Metal Plate
CALL( "elements/specz.udo", spm, 1, x, y, z-ch/2-mdz, 6 );
# Plane Wave Box
CALL( "elements/specx.udo", spplx1, 1, x-pld/2, y, z, 6 );
CALL( "elements/specx.udo", spplx2, 1, x+pld/2, y, z, 6 );
CALL( "elements/specy.udo", spply1, 1, x, y-pls/2, z, 6 );
CALL( "elements/specy.udo", spply2, 1, x, y+pls/2, z, 6 );
CALL( "elements/specz.udo", spplz1, 1, x, y, z-plw/2, 6 );
CALL( "elements/specz.udo", spplz2, 1, x, y, z+plw/2, 6 );

CLOSEOBJ;

```

## UDO Script for Sixteen-Cylinder Model

```
comment="16 AlN:Mo cylinders on a plate with set dimensions inside a  
plane wave box surrounded by NTF+ABC boxes";  
bitmap="AlNMoM.jpg";
```

```
PAR( "Plane wave port file name", plp, plw1 );  
PAR( "AlN:Mo cylinder: thickness (z-dir)", ch, 10 );  
PAR( "AlN:Mo cylinder: number of sectors", cn, 32 );  
PAR( "AlN:Mo cylinder: medium", cmed, AlN );  
PAR( "Spacing between cylinders", spc, 1 );  
PAR( "Metal plate: length (x- and y-dir)", mdx, 21 );  
PAR( "Metal plate: thickness (z-dir)", mdz, 1 );  
PAR( "Metal plate: medium", mmed, metal );  
PAR( "Cell size in air", cair, 0.295 );  
PAR( "Cell size in AlN:Mo cylinder", ccer, 0.095 );
```

```
ENDHEADER;
```

```
OPENOBJECT( plwntf3 );
```

```
MESHPAR ( cair, cair, cair, 1, 2, 1, 2, 1, 2, 1 );
```

```
cr = (mdx-3*spc)/8;
```

```
a = cr+0.5*spc;
```

```
# AlN:Mo cylinders
```

```
CALL( "elements/cyv.udo", cylobj1, cr, ch, cn, cmed, N, x-3*a, y+3*a,  
z-ch/2, 10 );
```

```
CALL( "elements/cyv.udo", cylobj2, cr, ch, cn, cmed, N, x-a, y+3*a,  
z-ch/2, 10 );
```

```
CALL( "elements/cyv.udo", cylobj3, cr, ch, cn, cmed, N, x+a, y+3*a,  
z-ch/2, 10 );
```

```
CALL( "elements/cyv.udo", cylobj4, cr, ch, cn, cmed, N, x+3*a, y+3*a,  
z-ch/2, 10 );
```

```
CALL( "elements/cyv.udo", cylobj5, cr, ch, cn, cmed, N, x-3*a, y+a,  
z-ch/2, 10 );
```

```
CALL( "elements/cyv.udo", cylobj6, cr, ch, cn, cmed, N, x-a, y+a,  
z-ch/2, 10 );
```

```

CALL( "elements/cyv.udo", cylobj7, cr, ch, cn, cmed, N, x+a, y+a,
      z-ch/2, 10 );
CALL( "elements/cyv.udo", cylobj8, cr, ch, cn, cmed, N, x+3*a, y+a,
      z-ch/2, 10 );
CALL( "elements/cyv.udo", cylobj9, cr, ch, cn, cmed, N, x-3*a, y-a,
      z-ch/2, 10 );
CALL( "elements/cyv.udo", cylobj10, cr, ch, cn, cmed, N, x-a, y-a,
      z-ch/2, 10 );
CALL( "elements/cyv.udo", cylobj11, cr, ch, cn, cmed, N, x+a, y-a,
      z-ch/2, 10 );
CALL( "elements/cyv.udo", cylobj12, cr, ch, cn, cmed, N, x+3*a, y-a,
      z-ch/2, 10 );
CALL( "elements/cyv.udo", cylobj13, cr, ch, cn, cmed, N, x-3*a, y-3*a,
      z-ch/2, 10 );
CALL( "elements/cyv.udo", cylobj14, cr, ch, cn, cmed, N, x-a, y-3*a,
      z-ch/2, 10 );
CALL( "elements/cyv.udo", cylobj15, cr, ch, cn, cmed, N, x+a, y-3*a,
      z-ch/2, 10 );
CALL( "elements/cyv.udo", cylobj16, cr, ch, cn, cmed, N, x+3*a, y-3*a,
      z-ch/2, 10 );

```

# Adjacent metal plate

```

CALL( "basic/cubo.udo", plateobj, mdx, mdx, mdz, mmed, E, 0, x, y,
      z-ch/2-mdz, 11 );

```

# NTF and ABC boxes

```

d = mdx+9;
s = mdx+9;
w = 24;

```

```

dh = 0.5*d;
sh = 0.5*s;
wh = 0.5*w;

```

```

dntf = mdx+6;
sntf = mdx+6;
wntf = 21;

```

```

CALL( "boxes/ntf.udo", d, s, w, dntf, sntf, wntf, N, N, N, x-dh, y-sh,

```

```

z-wh, 13 );

# Plane wave surfaces
pld = mdx+3;
pls = mdx+3;
plw = 18;

CALL( "boxes/plw_pure.udo", plwbox, pld, pls, plw, plp, x, y, z, 9 );

# SPs
# Mesh
CALL( "elements/specxu.udo", spx1, 1, ccer, x-mdx/2-0.5, y, z, 7 );
CALL( "elements/specxd.udo", spx2, 1, ccer, x+mdx/2+0.5, y, z, 7 );
CALL( "elements/specyu.udo", spy1, 1, ccer, x, y-mdx/2-0.5, z, 7 );
CALL( "elements/specyd.udo", spy2, 1, ccer, x, y+mdx/2+0.5, z, 7 );
CALL( "elements/speczu.udo", spz1, 1, ccer, x, y, z-ch/2, 7 );
CALL( "elements/speczd.udo", spz2, 1, ccer, x, y, z+ch/2+0.5, 7 );
CALL( "elements/specx.udo", spx1, 1, x-mdx/2, y, z, 6 );
CALL( "elements/specx.udo", spx2, 1, x+mdx/2, y, z, 6 );
CALL( "elements/specy.udo", spy1, 1, x, y-mdx/2, z, 6 );
CALL( "elements/specy.udo", spy2, 1, x, y+mdx/2, z, 6 );
CALL( "elements/specz.udo", spz1, 1, x, y, z-ch/2, 6 );
CALL( "elements/specz.udo", spz2, 1, x, y, z+ch/2, 6 );
# Cylinder 1
CALL( "elements/specx.udo", spc1x, 1, x-(a+spc+cr), y+3*a, z, 6 );
CALL( "elements/specy.udo", spc1y, 1, x-3*a, y+(a+spc+cr), z, 6 );
# Cylinder 2
CALL( "elements/specx.udo", spc2x1, 1, x-(a+cr), y+3*a, z, 6 );
CALL( "elements/specx.udo", spc2x2, 1, x-(a-cr), y+3*a, z, 6 );
CALL( "elements/specy.udo", spc2y, 1, x-a, y+(a+spc+cr), z, 6 );
# Cylinder 3
CALL( "elements/specx.udo", spc3x1, 1, x+(a+cr), y+3*a, z, 6 );
CALL( "elements/specx.udo", spc3x2, 1, x+(a-cr), y+3*a, z, 6 );
CALL( "elements/specy.udo", spc3y, 1, x+a, y+(a+spc+cr), z, 6 );
# Cylinder 4
CALL( "elements/specx.udo", spc4x, 1, x+(a+spc+cr), y+3*a, z, 6 );
CALL( "elements/specy.udo", spc4y, 1, x+3*a, y+(a+spc+cr), z, 6 );
# Cylinder 5
CALL( "elements/specx.udo", spc5x, 1, x-(a+spc+cr), y+a, z, 6 );

```

```

CALL( "elements/specy.udo", spc5y1, 1, x-3*a, y+(a+cr), z, 6 );
CALL( "elements/specy.udo", spc5y2, 1, x-3*a, y+(a-cr), z, 6 );
# Cylinder 6
CALL( "elements/specx.udo", spc6x1, 1, x-(a+cr), y+a, z, 6 );
CALL( "elements/specx.udo", spc6x2, 1, x-(a-cr), y+a, z, 6 );
CALL( "elements/specy.udo", spc6y1, 1, x-a, y+(a+cr), z, 6 );
CALL( "elements/specy.udo", spc6y2, 1, x-a, y+(a-cr), z, 6 );
# Cylinder 7
CALL( "elements/specx.udo", spc7x1, 1, x+(a+cr), y+a, z, 6 );
CALL( "elements/specx.udo", spc7x2, 1, x+(a-cr), y+a, z, 6 );
CALL( "elements/specy.udo", spc7y1, 1, x+a, y+(a+cr), z, 6 );
CALL( "elements/specy.udo", spc7y2, 1, x+a, y+(a-cr), z, 6 );
# Cylinder 8
CALL( "elements/specx.udo", spc8x, 1, x+(a+spc+cr), y+a, z, 6 );
CALL( "elements/specy.udo", spc8y1, 1, x+3*a, y+(a+cr), z, 6 );
CALL( "elements/specy.udo", spc8y2, 1, x+3*a, y+(a-cr), z, 6 );
# Cylinder 9
CALL( "elements/specx.udo", spc9x, 1, x-(a+spc+cr), y-a, z, 6 );
CALL( "elements/specy.udo", spc9y1, 1, x-3*a, y-(a+cr), z, 6 );
CALL( "elements/specy.udo", spc9y2, 1, x-3*a, y-(a-cr), z, 6 );
# Cylinder 10
CALL( "elements/specx.udo", spc10x1, 1, x-(a+cr), y-a, z, 6 );
CALL( "elements/specx.udo", spc10x2, 1, x-(a-cr), y-a, z, 6 );
CALL( "elements/specy.udo", spc10y1, 1, x-a, y-(a+cr), z, 6 );
CALL( "elements/specy.udo", spc10y2, 1, x-a, y-(a-cr), z, 6 );
# Cylinder 11
CALL( "elements/specx.udo", spc11x1, 1, x+(a+cr), y-a, z, 6 );
CALL( "elements/specx.udo", spc11x2, 1, x+(a-cr), y-a, z, 6 );
CALL( "elements/specy.udo", spc11y1, 1, x+a, y-(a+cr), z, 6 );
CALL( "elements/specy.udo", spc11y2, 1, x+a, y-(a-cr), z, 6 );
# Cylinder 12
CALL( "elements/specx.udo", spc12x, 1, x+(a+spc+cr), y-a, z, 6 );
CALL( "elements/specy.udo", spc12y1, 1, x+3*a, y-(a+cr), z, 6 );
CALL( "elements/specy.udo", spc12y2, 1, x+3*a, y-(a-cr), z, 6 );
# Cylinder 13
CALL( "elements/specx.udo", spc13x, 1, x-(a+spc+cr), y-3*a, z, 6 );
CALL( "elements/specy.udo", spc13y, 1, x-3*a, y-(a+spc+cr), z, 6 );
# Cylinder 14
CALL( "elements/specx.udo", spc14x1, 1, x-(a+cr), y-3*a, z, 6 );

```

```

CALL( "elements/specx.udo", spc14x2, 1, x-(a-cr), y-3*a, z, 6 );
CALL( "elements/specy.udo", spc14y, 1, x-a, y-(a+spc+cr), z, 6 );
# Cylinder 15
CALL( "elements/specx.udo", spc15x1, 1, x+(a+cr), y-3*a, z, 6 );
CALL( "elements/specx.udo", spc15x2, 1, x+(a-cr), y-3*a, z, 6 );
CALL( "elements/specy.udo", spc15y, 1, x+a, y-(a+spc+cr), z, 6 );
# Cylinder 16
CALL( "elements/specx.udo", spc16x, 1, x+(a+spc+cr), y-3*a, z, 6 );
CALL( "elements/specy.udo", spc16y, 1, x+3*a, y-(a+spc+cr), z, 6 );
# Top and Bottom of Cylinders
CALL( "elements/specz.udo", spm, 1, x, y, z-ch/2, 6 );
CALL( "elements/specz.udo", spm, 1, x, y, z+ch/2, 6 );
# Bottom of Metal Plate
CALL( "elements/specz.udo", spm, 1, x, y, z-ch/2-mdz, 6 );
# Plane Wave Box
CALL( "elements/specx.udo", spplx1, 1, x-pld/2, y, z, 6 );
CALL( "elements/specx.udo", spplx2, 1, x+pld/2, y, z, 6 );
CALL( "elements/specy.udo", spply1, 1, x, y-pls/2, z, 6 );
CALL( "elements/specy.udo", spply2, 1, x, y+pls/2, z, 6 );
CALL( "elements/specz.udo", spplz1, 1, x, y, z-plw/2, 6 );
CALL( "elements/specz.udo", spplz2, 1, x, y, z+plw/2, 6 );

CLOSEOBJ;

```

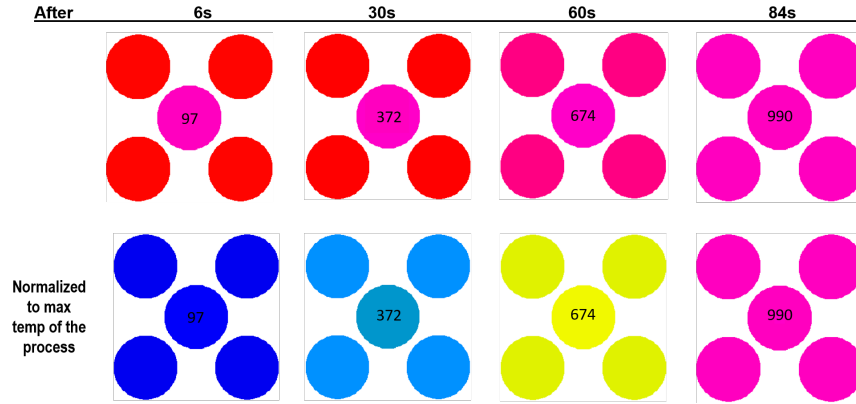
## B Temperature Field Patterns in Five-Cylinder Model

Temperature field patterns were simulated in the five-cylinder system for all six concentrations of Mo in the AlN:Mo composite. The temperature patterns for each concentration were captured at four different time steps. The first temperature patterns were taken after the first time step (time steps varied by simulation), whereas the initial temperatures in all models was 25 °C. The final temperature patterns were taken in the time step just before the model hit 1 000 °C.

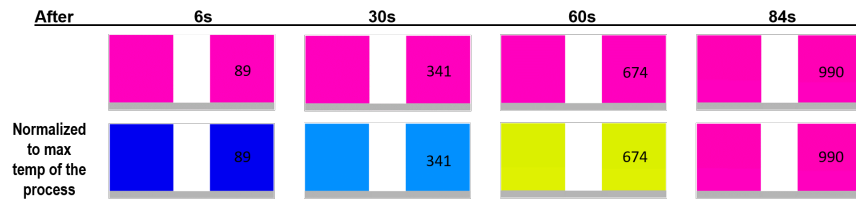
For each AlN:Mo composite, temperature patterns were taken in the  $xy$ -plane along the surface adjacent to the metal baseplate as well as in the  $xz$ -plane through the centers of two of the outer cylinders. Figure B.1 shows the temperature scale for the temperature distributions within the heating process. All temperature patterns are represented in Figures B.2 through B.7.



Figure B.1: Temperature scale for patterns of temperature distribution in AlN:Mo susceptors.

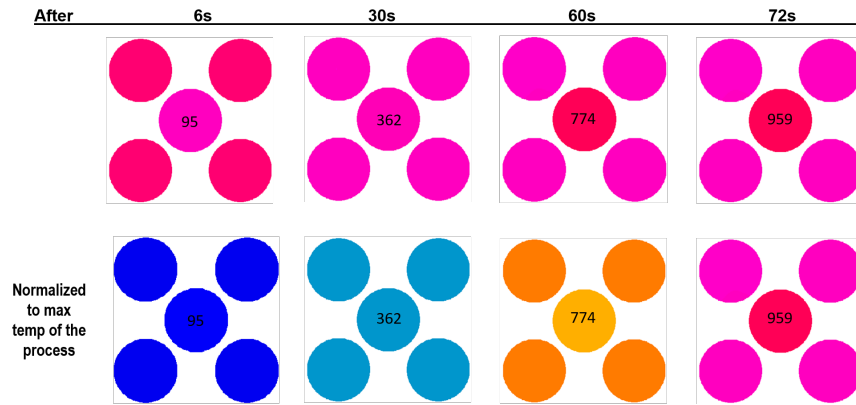


(a)

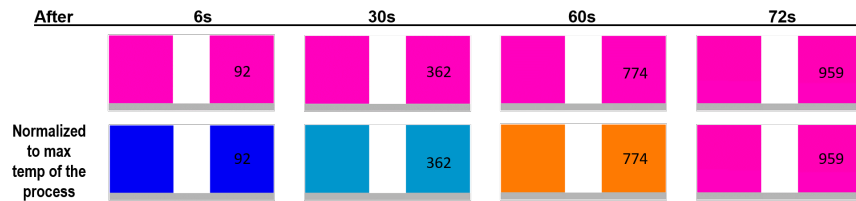


(b)

Figure B.2: Temperature patterns in the  $xy$ -plane along the surface adjacent to the baseplate (a) and in the  $xz$ -plane (b) for 0.25% Mo.



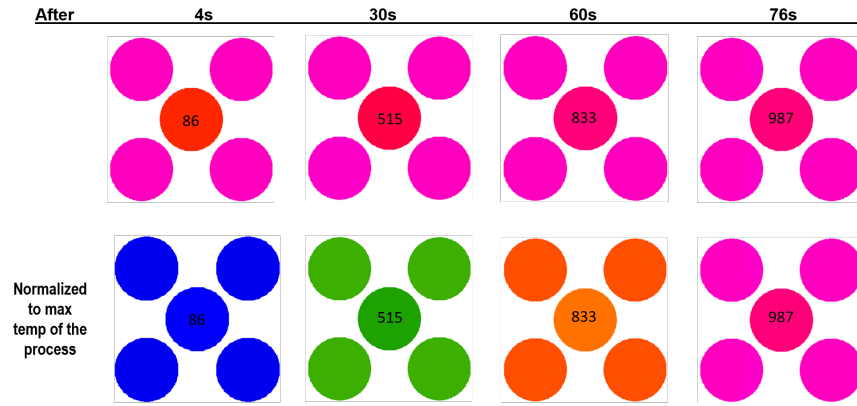
(a)



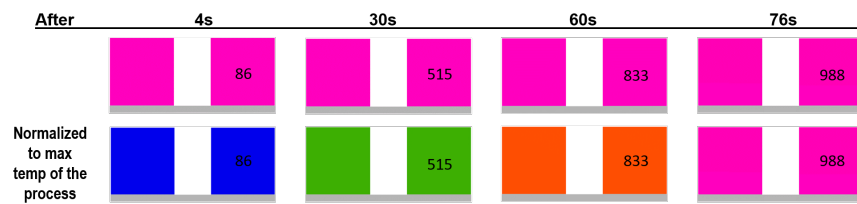
(b)

Figure B.3: Temperature patterns in the  $xy$ -plane along the surface adjacent to the baseplate (a) and in the  $xz$ -plane (b) for 0.5% Mo.



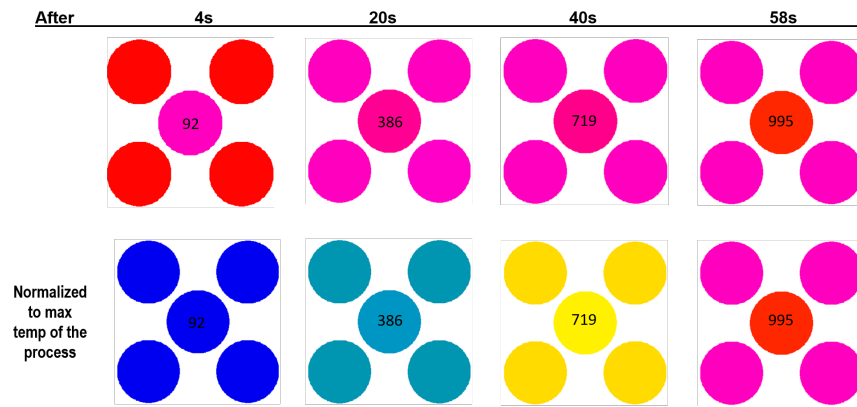


(a)

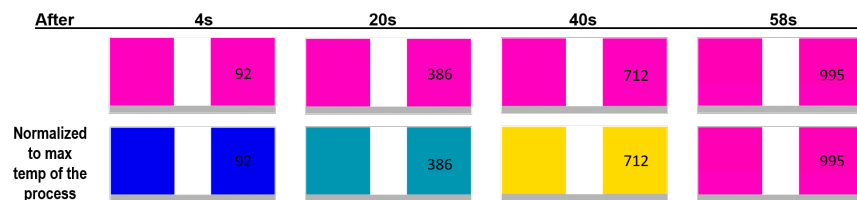


(b)

Figure B.4: Temperature patterns in the  $xy$ -plane along the surface adjacent to the baseplate (a) and in the  $xz$ -plane (b) for 1.0% Mo.

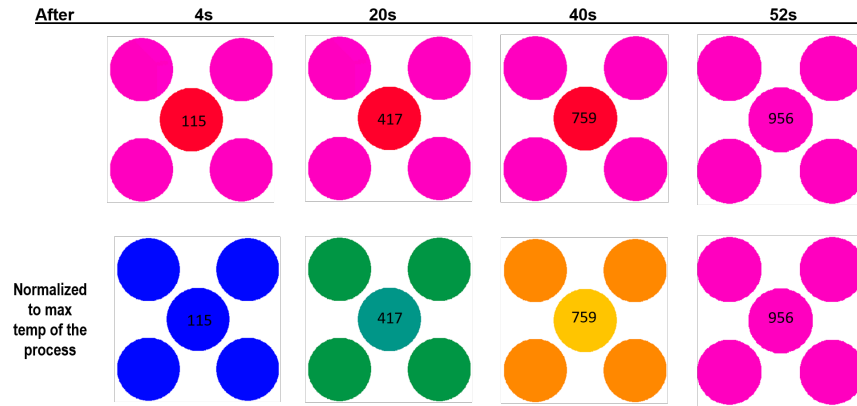


(a)

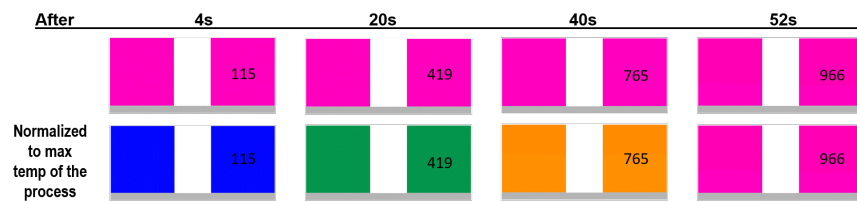


(b)

Figure B.5: Temperature patterns in the  $xy$ -plane along the surface adjacent to the baseplate (a) and in the  $xz$ -plane (b) for 2.0% Mo.

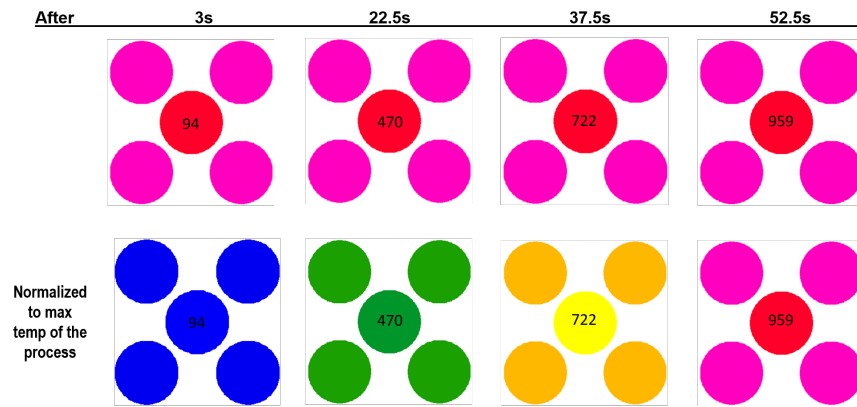


(a)

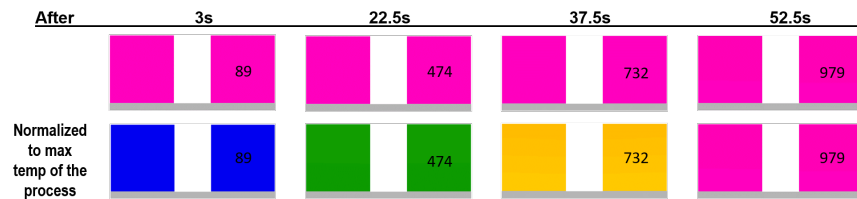


(b)

Figure B.6: Temperature patterns in the  $xy$ -plane along the surface adjacent to the baseplate (a) and in the  $xz$ -plane (b) for 3.0% Mo.



(a)



(b)

Figure B.7: Temperature patterns in the  $xy$ -plane along the surface adjacent to the baseplate (a) and in the  $xz$ -plane (b) for 4.0% Mo.

## C Calculation of Exposed Surface Areas Based on Angle of Incidence

The application of MMW HXs in real-world scenarios will face additional challenges when it comes to the angle of incidence of the incoming plane wave. Outside of computational tests, it won't be possible to maintain perfect normal incidence. Corresponding simulations are therefore required to study the impact of angle of incidence on the performance of the device. Within *QuickWave*, input parameters used in defining the power of the incoming EM field are set up in Watts, while the characterization of energy efficiency of the MMW HX requires the use of power density, which is calculated using the area of the susceptors exposed to the field. The calculation of this area is simple in scenarios with normal incidence, but becomes more complex in the case of off-normal incidence, especially with multiple susceptors. In this Appendix, an equation is derived for the calculation of exposed surface area to be used in determining the power density of future computational studies on the effect of the off-normal incidence of the plane wave onto cylindrical absorbing elements.

In the case of a multi-cylinder model, only the models where the number of cylinders is a perfect square number are considered (the 4-, 9-, and 16-cylinder models), as the 5-cylinder model proved too complex to accurately approximate the exposed surface area. In the event that a circle of radius  $r$  is viewed from an angle  $0 \leq \theta < 90^\circ$ , where  $\theta = 0^\circ$  is directly perpendicular to the circle, the circle becomes an ellipse with semi-major axis  $r_1 = r$  and semi-minor axis  $r_2 = r \cos \theta$ . As such, the exposed surface area of the multi-cylinder systems can be calculated using properties of ellipses.

When calculating the exposed surface area, there are two scenarios to consider: when the cylinders do not overlap one another (the surface area of a cylinder is covering a portion of another cylinder), and when the cylinders do overlap one another. Whether or not the cylinders overlap depend on the angle of incidence  $\theta$ , the height of the cylinder  $h$ , and the spacing between cylinders  $s$ , pictured in Figure C.1. The overlap occurs when the incidence angle  $\theta$  is larger than the inverse tangent of the space between cylinders divided by the height of the cylinders ( $\theta > \tan^{-1}(\frac{s}{h})$ ). If there is no overlap, the total exposed surface area is equal to the exposed surface area of a single cylinder times the number of cylinders. If there is overlap, then this overlapping area must be subtracted from the total surface area.

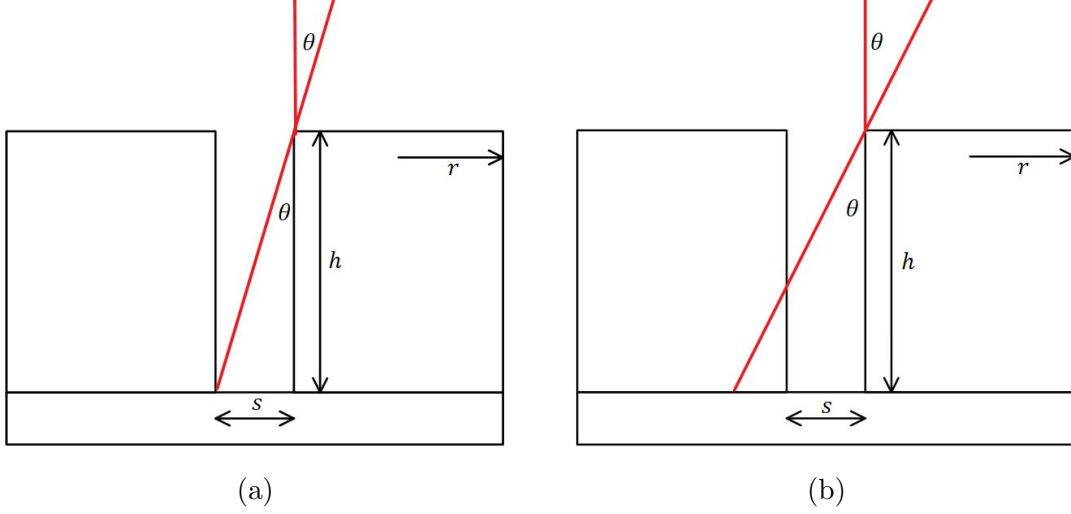


Figure C.1: Four-cylinder model with incidence angle  $\theta$ : no overlap in exposed surface area (a); some overlap in exposed surface area (b).

To find the exposed surface area  $A_c$  of a single cylinder, we find the surface area  $A_e$  of the ellipse and add it to the surface area of the side of the cylinder that is exposed to the incident wave. This is calculated using the approximate circumference  $c_e$  of the ellipse and the value  $t = h \tan \theta$ , which is the apparent height of the cylinder when viewed from angle  $\theta$ , shown in Figure C.2. Thus, the total exposed surface area of a single cylinder with a wave of incidence angle  $\theta$  (where  $0 \leq \theta < 90^\circ$ ) is

$$A_c = A_e + \frac{1}{2} (tc_e), \quad (4)$$

where

$$A_e = \pi r_1 r_2 = \pi r r \cos \theta = \pi r^2 \cos \theta,$$

$$c_e = 2\pi \sqrt{\frac{r_1^2 + r_2^2}{2}} = 2\pi \sqrt{\frac{r^2 + (r \cos \theta)^2}{2}}.$$

In the case where the angle of incidence is greater than  $\tan^{-1}(\frac{s}{h})$ , the area of overlapping cylinders must also be considered. To do so, we use the identical ellipses which are the top of the cylinder in front and the base of the cylinder in back, pictured in Figure C.3. The intersection points of these ellipses can be found by creating a coordinate system with  $(0,0)$  at the center of the top of the cylinder in front. These ellipses can then be written as

$$\frac{x^2}{r_1^2} + \frac{y^2}{r_2^2} = 1, \quad (5)$$

$$\frac{x^2}{r_1^2} + \frac{(y - (2r_2 - o))^2}{r_2^2} = 1. \quad (6)$$

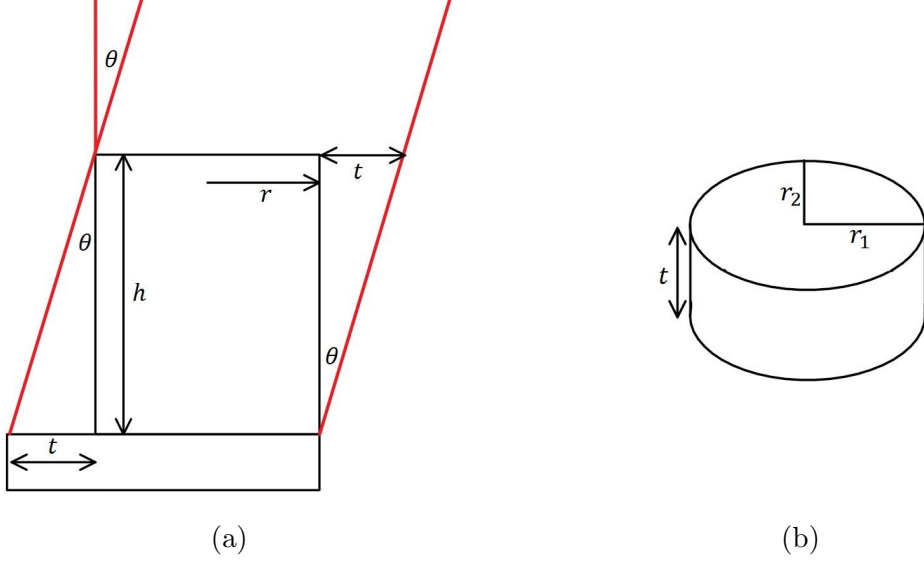


Figure C.2: Exposed surface area of single cylinder with incidence angle  $\theta$ : view of the side (a); view of the top from incidence angle  $\theta$  (b).

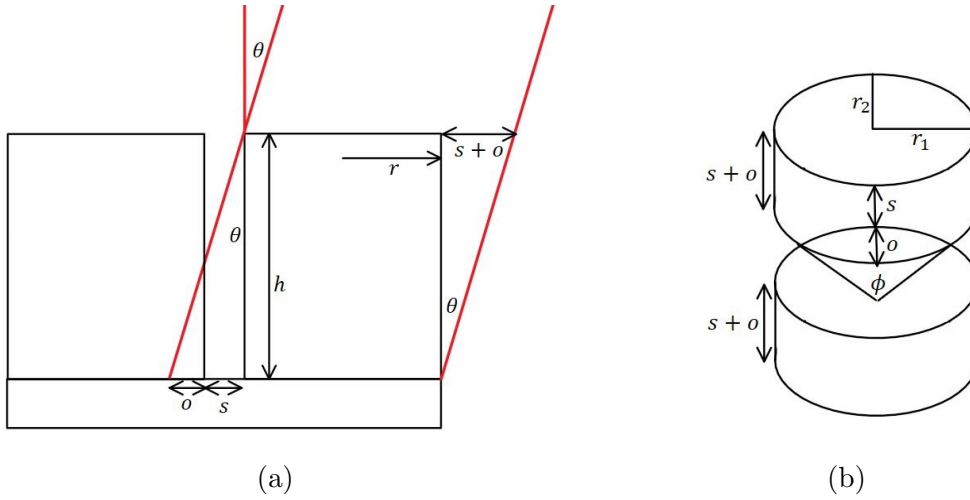


Figure C.3: Exposed surface area of two overlapping cylinders with incidence angle  $\theta$ : view of the side (a); view of the top from incidence angle  $\theta$  (b).

In this scenario, the apparent height  $t$  of the cylinder is the sum of the space  $s$  between the cylinders and the amount of overlap  $o$ . Finding the area  $A_o$  of the overlapping region is done by using the angle  $\phi$  between the two intersection points to find the area of the sector of the ellipse and the area of an isosceles triangle generated by the intersection points and the center of the ellipse. To find the points of intersection between these ellipses, we subtract (6) from (5) and solve for  $y$ , and solve for  $x$  by plugging this  $y$  value into (5).

$$y = r_2 - \frac{o}{2}, \tag{7}$$

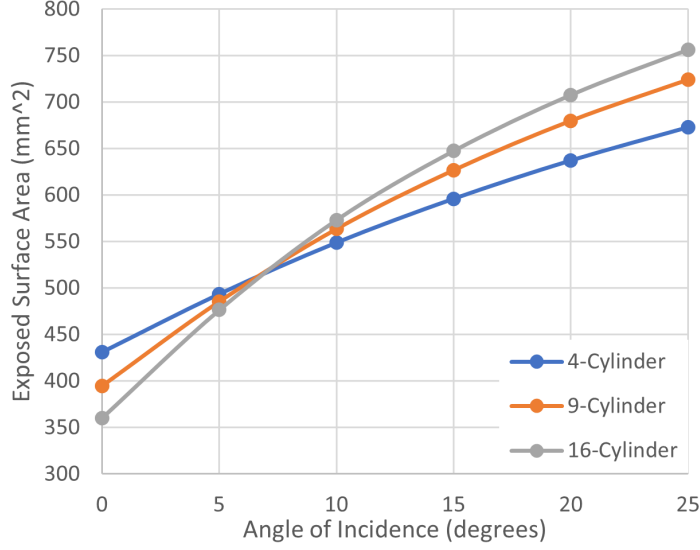


Figure C.4: Exposed surface area of multi-cylinder models as a function of angle of incidence.

$$x = \pm \sqrt{r_1^2 - \frac{r_1^2}{r_2^2} \left( r_2 - \frac{o}{2} \right)^2}. \quad (8)$$

The angle  $\phi$  of the sectors of each ellipses generated by these intersection points is found using (7) and (8)

$$\phi = 2 \tan^{-1} \left( \frac{x}{y} \right), \quad (9)$$

which can be split into  $\phi_1 = \frac{\pi}{2} - \frac{\phi}{2}$  and  $\phi_2 = \frac{\pi}{2} + \frac{\phi}{2}$  such that  $\phi = \phi_2 - \phi_1$ . Then the area  $A_s$  of the sector is given by

$$A_s = F(\phi_2) - F(\phi_1), \quad (10)$$

where

$$F(\phi) = \frac{r_1 r_2}{2} \left( \phi - \tan^{-1} \left( \frac{(r_2 - r_1) \sin(2\phi)}{r_1 + r_2 + (r_2 - r_1) \cos(2\phi)} \right) \right).$$

Once  $A_s$  is found, the area of the overlapping region can be found using the area  $A_t$  of the triangle created by the center of the ellipse and the two intersection points from (7) and (8):

$$A_t = xy \quad (11)$$

Thus, the final formula for the area  $A_o$  of the overlapping region of two cylinders is given by

$$A_o = 2(A_s - A_t). \quad (12)$$

To find the total exposed surface area  $A$  of the entire multi-cylinder model with  $n$  cylinders, we multiply the total number of cylinders by the total exposed surface area  $A_c$  of a single cylinder (from (4)) and subtract the number of cylinders partially covered by another cylinder by the area  $A_o$  of the overlapping region (from (12)), giving the final formula

$$A = nA_c - \sqrt{n}(\sqrt{n} - 1) A_o \quad (13)$$

This final formula (13) and all necessary calculations leading up to it were turned into a MATLAB script which takes in an incidence angle  $\theta$  (where  $0 \leq \theta < 90^\circ$ ) and a number of cylinders  $n$  (where  $n$  must be a square number) and outputs an approximate total exposed surface area  $A$ . The MATLAB script is presented in Appendix D.

Preliminary calculations using 13 generated values of the exposed surface area in the four-, nine-, and sixteen-cylinder models for incidence angles of  $0^\circ$ ,  $5^\circ$ ,  $10^\circ$ ,  $15^\circ$ ,  $20^\circ$ , and  $25^\circ$ . Figure C.4 shows a graph of these values of surface areas as functions of the angle of incidence.

## D Exposed Surface Area MATLAB Script

Following the derivation of the formula for the exposed surface area of a multi-cylinder model when viewed from off-normal incidence (Appendix C), a MATLAB script was generated which allows a user to input the angle of incidence and the number of cylinders in the model and calculate the exposed surface area. This MATLAB script is presented below.

```
1 % Calculation of Exposed Surface Area by Angle of Incidence
2
3 %% Input Information About Model
4 % Input number of cylinders
5 n = input('Number of cylinders (must be a square number): ');
6 % Check if input is valid
7 if floor(sqrt(n)).^2 ~= n
8     fprintf('\n Error: number of cylinders must be square number \n');
9     n = input('Number of cylinders (must be a square number): ');
10 else
11     n = n;
12 end
13 % Input angle of incidence
14 theta = input('Angle of incidence (in degrees): ');
15 % Check if input is valid
16 if theta >= 90
17     fprintf('\n Error: angle of incidence must be less than 90 \n \n');
18     theta = input('Angle of incidence (in degrees): ');
19 else
20     theta = theta;
21 end
22 % Known values
23 h = 10; % Height of cylinder
24 s = 1; % Space between cylinders
25 r5 = 4.765; % Radius of cylinder in 5-cylinder model
26 L = (1 / sqrt(2)) * ((2 * s) + (2 * sqrt(2) * r5) + (4 * r5)); % Length of metal plate
27 theta = theta * (pi / 180); % Angle of incidence in radians
28
29 %% Radii of Ellipse
30 r1 = (L - ((sqrt(n) - 1) * s)) / (2 * sqrt(n)); % Semi-major axis
31 if r1 <= 0
32     fprintf('\n Error: too many cylinders \n \n');
33     return
```



```

34 end
35 r2 = r1 * cos(theta); % Semi-minor axis
36
37 %% Exposed Surface Area of One Cylinder
38 t = 10 * tan(theta); % Thickness of cylinder exposed
39 c = 2 * pi * sqrt(((r1^2) + (r2^2)) / 2); % Circumference of ellipse
40 Ae = pi * (r1^2) * cos(theta); % Area of ellipse
41 Ac = Ae + (t * 0.5 * c); % Exposed surface area of one cylinder
42
43 %% Area of overlapping region
44 if t > s % Check if the cylinders overlap
45     o = t - s; % Length of overlapping region
46     y = r2 - (o / 2); % y-coordinate of intersection point
47     x = sqrt((r1^2) - (((r1^2) * (y^2)) / (r2^2))); % x-coordinate of intersection point
48     phi = 2 * atan(x / y); % Angle of sector
49     phi1 = (pi / 2) - (phi / 2);
50     phi2 = (pi / 2) + (phi / 2);
51     F1 = ((r1 * r2) / 2) * (phi1 - atan(((r2 - r1) * sin(2 * phi1)) / (r2 + r1 + ((r2 - r1)
52         * cos(2 * phi1)))));
53     F2 = ((r1 * r2) / 2) * (phi2 - atan(((r2 - r1) * sin(2 * phi2)) / (r2 + r1 + ((r2 - r1)
54         * cos(2 * phi2)))));
55     As = F2 - F1; % Area of sector
56     At = x * (r2 - (o / 2)); % Area of triangle
57     Ao = 2 * (As - At); % Area of overlapping region
58 else
59     Ao = 0; % Area of overlapping region is 0 (no overlap)
60 end
61
62 %% Total Exposed Surface Area
63 A = (n * Ac) - (sqrt(n) * (sqrt(n) - 1) * Ao);
64 fprintf('\n Total exposed surface area: %.2f mm^2 \n', A);

```

# E Computational Tests of Thermal Boundary Conditions

Following Section 6.3, this Appendix shows the output of computational experiments for explicit and adiabatic BCs ((1) and (2), respectively), for a model similar to the one of a MMW HX with a single rectangular block, but for zirconia as the absorbing material of a 100 mm cube and frequency 2.45 GHz.

Figures E.1 and E.2 show the temperature patterns and maximum temperatures in the zirconia cube on the central  $xz$ - and  $yz$ -planes respectively. Each figure shows 16 patterns, eight for the adiabatic BCs and eight for the explicit BCs. Patterns and timestamps are recorded when the processes reach particular time instances indicated in the figures.

The temperature patterns and values of maximum temperature show very little impact from the different BCs. In the model with adiabatic BCs, the maximum temperature of 324°C was reached in 123 seconds, while the model with explicit BCs took 142 seconds (an increase of 19 seconds). The temperature patterns are nearly identical between the adiabatic and explicit BCs; the only difference in the two sets of patterns is a dark blue outline on each of the temperature patterns with explicit BCs, which is caused by the boundaries being maintained at a constant low temperature of 25°C.

Figures E.3 and E.4 show the temperature patterns and maximum temperatures in the zirconia cube on the outermost  $xz$ - and  $yz$ -planes respectively. For the  $xz$ -plane, this is the right face of the cube (the left face of the cube showed identical patterns and values). For the  $yz$ -plane, this is the front face of the cube (the back face of the cube showed identical patterns and values). For the outermost planes, only the patterns and values from the final time-step, where the maximum temperature is 324°C, are pictured. Each figure shows four patterns, two for the adiabatic BCs and two for the explicit BCs. Patterns are shown in two ways, non-normalized and normalized to 324°C.

The impact of  $h$  on the temperature at the faces of the cube are similar to the impact of  $h$  on the temperature at the center of the cube. Once again, the temperature patterns are nearly identical between the adiabatic and explicit BCs; the only difference in the two sets of patterns is a dark blue outline on each of the temperature patterns with explicit BCs, which is caused by the

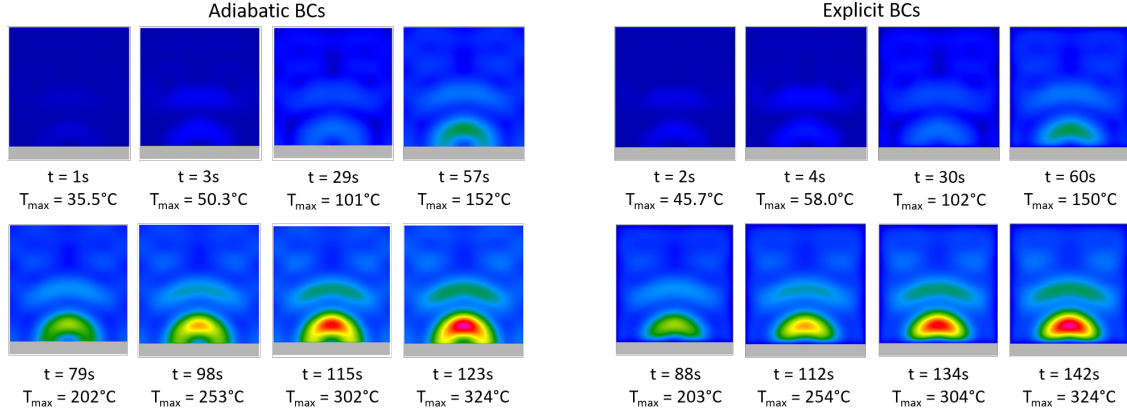


Figure E.1: Temperature patterns in the zirconia cube on the  $xz$ -plane through center.

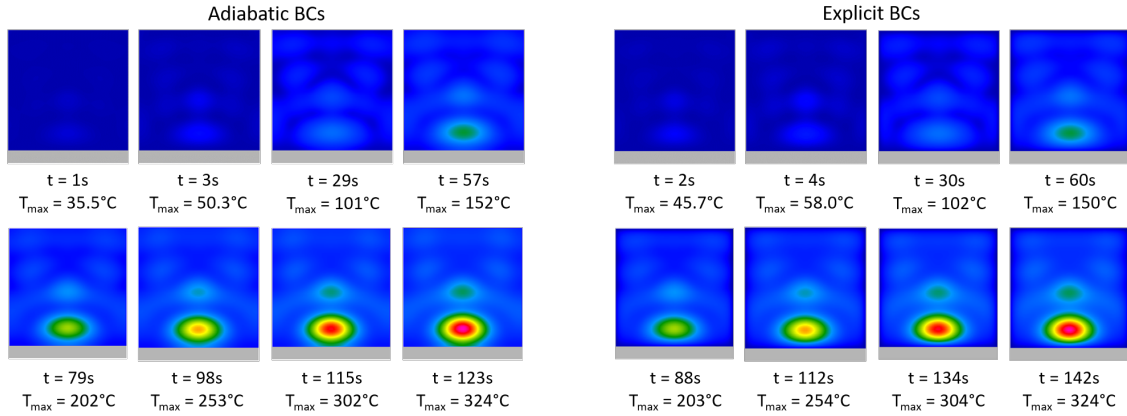


Figure E.2: Temperature patterns in the zirconia cube on the  $yz$ -plane through center.

boundaries being maintained at a constant  $25^{\circ}\text{C}$ . The simulation records temperature patterns and values as averages of the  $2 \times 2 \times 2$  mm cells closest to the edge of the cube, and not just the values on the exact boundary. This is why the patterns in the explicit boundary conditions do not show a constant  $25^{\circ}\text{C}$  across the entire plane.

The most significant differences between the two cases occur at the boundary between the ceramic cube and the metal plate. Similar to the faces of the cube, it again seen that the patterns in the explicit boundary conditions do not show a constant  $25^{\circ}\text{C}$  across the entire plane due to the size of the cells at the boundaries. Figure E.5 shows this boundary for both cases, and the temperature patterns are normalized to  $324^{\circ}\text{C}$ , the maximum temperature in the entire cube. In Figure E.6, the temperature patterns are normalized to the respective maximum temperatures of each case.

In the case with the adiabatic BCs, the maximum temperature on the boundary between the ceramic block and the metal plate is  $225^{\circ}\text{C}$ . For the case with the explicit BCs, the maximum temperature is  $71.0^{\circ}\text{C}$ . This is a difference of  $154^{\circ}\text{C}$ , meaning that switching from adiabatic BCs

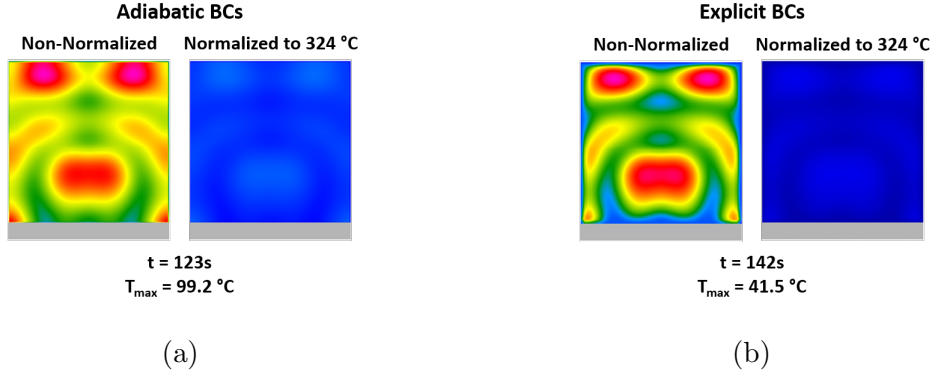


Figure E.3: Temperature patterns in the zirconia cube on the  $xz$ -plane on right face with adiabatic (a) and explicit (b) BCs.

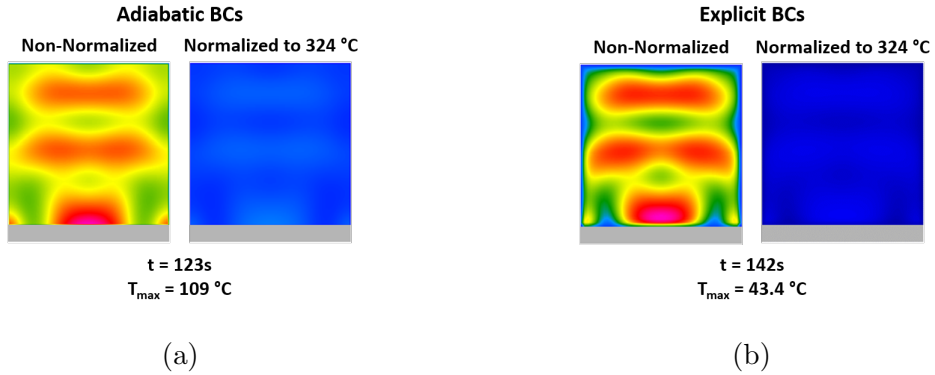


Figure E.4: Temperature patterns in the zirconia cube on the  $yz$ -plane on front face with adiabatic (a) and explicit (b) BCs.

to explicit BCs reduces the maximum temperature at this specific boundary by 68.4%.

The lack of visible effect produced by the difference in the explicit and adiabatic BCs appears suggests that for the AlN:Mo composite at 95 GHz, the results could be different. The differences may be due to different material parameters and frequencies of the two scenarios. As such, the presented computational test for zirconia may therefore be seen inconclusive. It is recommended that the issue of the impact of thermal BCs on the output of the FDTD model be paid additional attention in the future computational studies of the MMW HX.

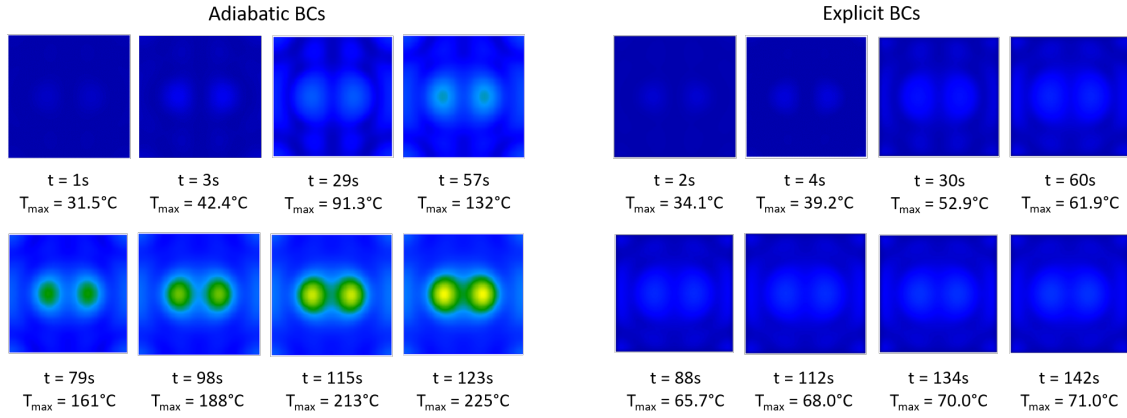


Figure E.5: Temperature patterns in the zirconia cube on the  $xy$ -plane adjacent to metal plate (normalized to  $324^{\circ}\text{C}$ ).

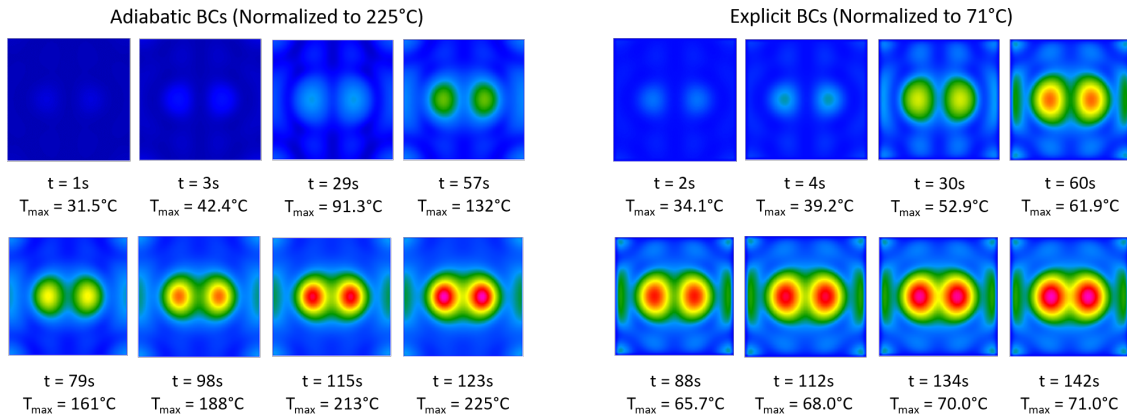


Figure E.6: Temperature patterns in the zirconia cube on the  $xy$ -plane adjacent to metal plate (normalized to respective  $T_{\max}$ ).

## F Determining Convective Heat Transfer Coefficient

As mentioned in Section 6.3 and Appendix E, the convective heat transfer coefficient is material property that greatly impacts the temperature flow in the MMW HX. In particular, it is used in (3) from Section 6.3 to determine the temperature of the susceptor in scenarios with convective BCs. In modeling practical scenarios, the convective heat transfer coefficient  $h$  should be set up in the model as an input parameters. Due to substantial difficulty in experimental determination of  $h$  for different real-life situations, it is feasible to have approximate values of  $h$  obtained from an empirical physical consideration. This Appendix shows a possible way of estimating  $h$  for the interface between air and a ceramic material.

Physically, the convective heat transfer coefficient  $h$  is the rate of heat transfer between a solid surface and a fluid per unit surface area per unit temperature difference [32]. It is an integral value used in the study of heat transfer, and can be very difficult to calculate or approximate. Empirical correlations between the mean heat transfer coefficient  $\bar{h}$  and the material properties of the air and the ceramic, listed in Table F.1, are focused around one specific property: the mean Nusselt number  $\overline{Nu}$  across a ceramic of height  $H$  [33]. The Nusselt number is a dimensionless temperature gradient at the surface, and it provides a measure of the convection heat transfer occurring at the surface [32]. There are a handful of methods used in determining the value, and these can be used to draw correlations between other material parameters. The two relations used in determining  $\bar{h}$  are [32,33]

$$\overline{Nu}_H = \frac{\bar{h}H}{k} \quad (14)$$

$$\overline{Nu}_H = \left( 0.825 + \frac{0.387Ra_H^{\frac{1}{6}}}{\left[ 1 + \left( \frac{0.492}{Pr} \right)^{\frac{9}{16}} \right]^{\frac{8}{27}}} \right)^2 \quad (15)$$

The parameters in (14) and (15) are introduced in Table F.1. Using (14) and (15), along with the derived properties the Rayleigh number  $Ra$  across a ceramic of height  $H$  and the Prandtl

Table F.1: Material Properties Used in Determining Convective Heat Transfer Coefficient

Variable	Material	Description	Equivalence	Units
$c_p$	Air	specific heat at constant pressure	$\frac{k}{\alpha\rho}, \frac{k\nu}{\alpha\mu}$	$\frac{\text{J}}{\text{kg}\cdot\text{K}}$
$g$	Air	acceleration due to gravity	N/A	$\frac{\text{m}}{\text{s}^2}$
$H$	Ceramic	height of ceramic layer	N/A	m
$k$	Air	thermal conductivity	$\alpha\rho c_p, \frac{\alpha\mu c_p}{\nu}$	$\frac{\text{J}}{\text{m}\cdot\text{s}\cdot\text{K}}$
$T_s$	Ceramic	surface temperature of ceramic	N/A	$K$
$T_A$	Air	ambient air temperature	$\frac{1}{\beta}$	$K$
$\alpha$	Air	thermal diffusivity	$\frac{k}{\rho c_p}, \frac{k\nu}{\mu c_p}$	$\frac{\text{m}^2}{\text{s}}$
$\beta$	Air	thermal coefficient of expansion	$\frac{1}{T_a}$	$\frac{1}{K}$
$\mu$	Air	dynamic viscosity	$\nu\rho$	$\text{Pa}\cdot\text{s}$
$\nu$	Air	kinematic viscosity	$\frac{\mu}{\rho}$	$\frac{\text{m}^2}{\text{s}}$
$\rho$	Air	density	$\frac{\mu}{\nu}, \frac{k}{\alpha c_p}$	$\frac{\text{kg}}{\text{m}^3}$

number, a formula for the mean heat transfer coefficient can be derived as (16):

$$\bar{h} = \frac{k}{H} \left( 0.825 + \frac{0.387 Ra_H^{\frac{1}{6}}}{\left[ 1 + \left( \frac{0.492}{Pr} \right)^{\frac{9}{16}} \right]^{\frac{8}{27}}} \right)^2 \quad (16)$$

where

$$Ra_H = \frac{g\beta(T_s - T_A)H^3}{\nu\alpha} = \frac{g\rho\beta(T_s - T_A)H^3}{\mu\alpha} \quad (17)$$

$$Pr = \frac{\nu}{\alpha} = \frac{\mu c_p}{k} \quad (18)$$

are also based on different properties of the air and the ceramic material.

It is important to note that (16)-(18) are only valid for a simple case of constant temperature across a vertical plate. Thus, these relations only provide a rough estimate for the approximate heat transfer coefficient  $h$  of the scenarios addressed in this project. Determining  $h$  for exactly these

Material proerties of air		
Density	rho (kg/m^3)	1.17
Gravity constant	g_const (m/s^2)	9.81
Ambient air temperature	TA (Kelvins)	300
Coefficient of thermal expansion of air	beta (1/K)	0.003333333
Dyamic viscosity	mu (Pa*s)	1.40E-05
Specific heat at constant pressure	cp (J/kg*K)	1000
Thermal conductivity	k (W/mK)	0.02
Thermal diffusivity	alpha (m^2/s)	1.7094E-05
<b>Derived values</b>		
Prandtl No	Pr	7.00E-01
Rayleigh Nmuber	Ra	3.20E+07

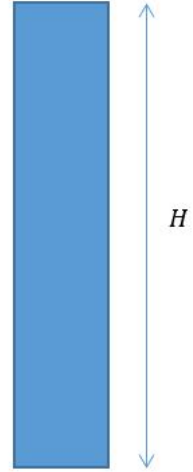
  

Material properties of ceramic		
Height of the cermic layer	H (in meters)	0.1
Surface temperature of the ceramic which is exposed to air	Ts (in kelvins)	500

Calculation of h		
This value will be automatically updated with changes in rest of the parameters	h (w/m^2 K)	8.708238877

Boundary exposed to air



A ceramic region

Figure F.1: Microsoft Excel spreadsheet which, in accordance with Table F.1, inputs the AlN:Mo material parameters  $\rho = 1.17 \frac{kg}{m^3}$ ,  $g = 9.81 \frac{m}{s^2}$ ,  $T = 300K$ ,  $\beta = 0.0333K^{-1}$ ,  $\mu = 1.40 \cdot 10^{-5} Pa s$ ,  $c_p = 1000 \frac{J}{kg K}$ ,  $k = 0.02 \frac{W}{m K}$ ,  $\alpha = 1.71 \cdot 10^{-5} \frac{m^2}{s}$ ,  $H = 0.1m$ , and  $T_s = 500K$  to produce the values  $Pr = 0.700$ ,  $Ra = 3.20 \cdot 10^7$ , and, finally,  $h = 8.71 \frac{W}{m^2 K}$

scenarios is a much more complex process, so the rough estimation of this parameter may be the only practical option in *QuickWave* modeling of MMW HX. Using (16) and the material properties of the AlN:Mo from [13], the value for  $h$  can be approximated and applied to further research.

A Microsoft Excel spreadsheet was made to calculate the value of  $h$  using (16) and the parameters from Table F.1. The contents of the spreadsheet is shown in Figure F.1



## G Plane Wave Incidence Settings in *QuickWave*

Within *QuickWave*, the plane wave incidence settings have three settings (Figure G.1) [18]:

- $\varphi$  (Phi): azimuthal angle of the direction of wave propagation
- $\vartheta$  (Theta): elevation angle of the direction of wave propagation
- Polarisation: polarisation angle of the electric field

By default, the above incidence settings of the plane wave are all set to  $0^\circ$ . This means that the plane wave comes from below and moves along the  $z$ -axis in the positive direction, orthogonal to the  $xy$ -plane. Adjusting the  $\varphi$  setting rotates the direction of the plane wave about the  $z$ -axis, and adjusting the  $\vartheta$  setting rotates the direction of the plane wave about the  $x$ -axis. Between these two angles, one can adjust the incidence settings to come from any direction. In all of the models with cylindrical susceptors, the angle  $\varphi$  was kept at  $0^\circ$  and the angle  $\vartheta$  was set to  $180^\circ$ , causing the plane wave to come from above and move along the  $z$ -axis in the negative direction, orthogonal to the  $xy$ -plane.

The final setting is the polarisation setting. This does not impact the direction that the wave comes from, but instead controls the orientation of the oscillations. In all simulations run for this project, the polarisation was set to  $0^\circ$ .

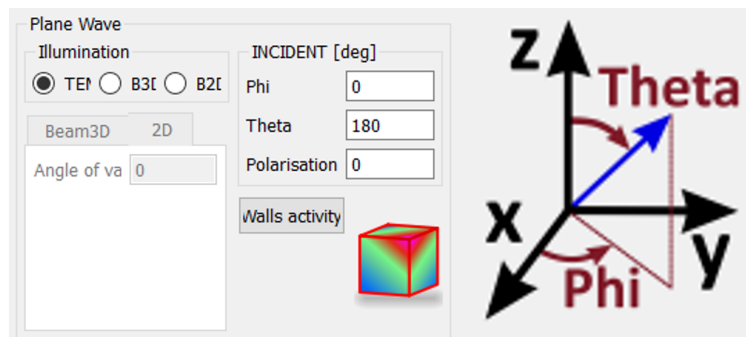


Figure G.1: Plane wave incidence settings in *QuickWave*.

# References

- [1] K. L. Parkin, D. L. D, and C. F. E, “The microwave thermal thruster concept,” *Proceedings of 2nd Beamed Energy Propulsion Symposium*, p. 418–429, 2004.
- [2] G. A. Landis, “Beamed energy propulsion for practical interstellar flight,” *Journal of the British Interplanetary Society*, vol. 52, pp. 420–423, 1999.
- [3] J. C. Coopersmith and E. Davis, “A strategic roadmap for commercializing low-cost beamed energy propulsion launch systems,” *Proceedings of American Institute of Aeronautics and Astronautics SPACE*, 2016.
- [4] A. Jamar, Z. Majid, W. Azmi, M. Norhafana, and A. Razak, “A review of water heating system for solar energy applications,” *International Communications in Heat and Mass Transfer*, vol. 76, pp. 178–187, 2016.
- [5] W. C. Brown and E. E. Eves, “Beamed microwave power transmission and its application to space,” *IEEE Transactions on Microwave Theory and Techniques*, vol. 40, pp. 1239–1250, June 1992.
- [6] J. N. Benford, “Space applications of high-power microwaves,” *IEEE Transactions on Plasma Science*, vol. 36, no. 3, pp. 569–581, 2008.
- [7] A. A. Mohekar, J. M. Gaone, B. S. Tilley, and V. V. Yakovlev, “A 2D coupled electromagnetic, thermal and fluid flow model: Application to layered microwave heat exchangers,” *Proceedings of IEEE MTT-S International Microwave Symposium*, pp. 1389–1392, 2018.
- [8] A. A. Mohekar, B. S. Tilley, and V. V. Yakovlev, “A 2d model of a triple layer electromagnetic heat exchanger with porous media flow,” *Proceedings of IEEE MTT-S International Microwave Symposium*, pp. 59–62, 2019.
- [9] A. A. Mohekar, B. S. Tilley, and V. V. Yakovlev, “Plane wave irradiation of a layered system: Resonance-based control over thermal runaway,” *Proceedings of 17th International Conference on Microwave and High Frequency Heating*, pp. 292–300, 2019.
- [10] B. Jawdat, B. W. Hoff, M. Hilario, A. Baros, P. Pelletier, T. Sabo, and F. W. Dynys, “Composite ceramics for power beaming,” *Proceedings of IEEE Wireless Power Transfer Conference*, 2017.
- [11] B. W. Hoff, M. S. Hilario, B. Jawdat, A. E. Baros, F. W. Dynys, J. A. Mackey, V. V. Yakovlev, C. E. Andraka, K. M. Armijo, E. Savrun, and I. M. Rittersdorf, “Millimeter wave interactions with high temperature materials and their applications to power beaming,” *Proceedings of 52nd IMPI’s Microwave Power Symposium*, pp. 82–83, June 2018.
- [12] P. Kumi, J. S. Venne, V. V. Yakovlev, M. S. Hilario, B. W. Hoff, and I. M. Rittersdorf, “Computational characterization of a composite ceramic block for a millimeter wave heat exchanger,” in *Scientific Computing in Electrical Engineering* (G. Nicosia and V. Romano, eds.), pp. 65–74, Springer, 2020.
- [13] P. Kumi, S. A. Martin, V. V. Yakovlev, M. S. Hilario, B. W. Hoff, and I. M. Rittersdorf, “Electromagnetic-thermal model of a millimeter-wave heat exchanger based on an AlN:Mo susceptor,” *COMPEL - The International Journal for Computation and Mathematics in Electrical and Electronic Engineering*, vol. 39, p. 481–496, Jan 2020.

- [14] I. M. Rittersdorf, B. W. Hoff, A. S. Richardson, S. A. Martin, V. V. Yakovlev, P. S. Kim, and J. W. Schumer, "A one-dimensional model for the millimeter-wave absorption and heating of dielectric materials in power beaming applications," *IEEE Transactions on Plasma Science*, vol. 49, no. 2, pp. 695–702, 2021.
- [15] S. Martin, *Computational Characterization of Thermal Processes in an AlN:Mo Susceptor in a Millimeter Wave Heat Exchanger*, Master's Thesis, Worcester Polytechnic Institute, 2019, p. 56.
- [16] J. M. Gaone, B. S. Tilley, and V. V. Yakovlev, "Electromagnetic heating control via high-frequency resonance of a triple-layer laminate," *Journal of Engineering Mathematics*, vol. 114, no. 1, pp. 65–86, 2019.
- [17] A. A. Mohekar, B. S. Tilley, and V. V. Yakovlev, "A triple layer electromagnetic heat exchanger with plane poiseuille flow: control and local onset of thermal runaway," *IEEE Journal on Multiscale and Multiphysics Computational Techniques*, vol. 5, pp. 119–131, 2020.
- [18] *QuickWave*, 1998-2021, QWED Sp. z.o.o. <https://www.qwed.com.pl>.
- [19] M. Goldberg, "The packing of equal circles in a square," *Mathematics Magazine*, vol. 43, no. 1, p. 24–30, 1970.
- [20] D. W. Boll, J. Donovan, R. L. Graham, and B. D. Lubachevsky, "Improving dense packings of equal disks in a square," *The Electronic Journal of Combinatorics*, vol. 7, no. R46, pp. 1–9, 2000.
- [21] C. D. Maranas, C. A. Floudas, and P. M. Pardalos, "New results in the packing of equal circles in a square," *Discrete Mathematics*, vol. 142, pp. 287–293, 1995.
- [22] Sienna Technologies, Inc. <http://siennatech.com/wp-content/uploads/2011/10/ST-200-AIN-Thermal-Conductivity.pdf>.
- [23] M. S. Hilario, B. W. Hoff, B. I. Jawdat, F. W. Dynys, and J. J. Wang, "High temperature millimeter-wave permittivity measurement setup for beamed energy heat exchangers," *Proceedings of 55th AIAA Aerospace Sciences Meeting*, 2017.
- [24] M. S. Hilario, B. W. Hoff, B. I. Jawdat, M. T. Lanagan, A. W. Cohick, F. W. Dynys, J. A. Mackey, and J. M. Gaone, "W-band complex permittivity measurements at high temperature using free-space methods," *IEEE Transactions on Components, Packaging, and Manufacturing Technology*, vol. 9, no. 6, pp. 1011–1019, 2019.
- [25] B. W. Hoff, M. S. Hayden, R. O. Grudt, F. W. Dynys, A. E. Baros, I. M. Rittersdorf, and M. L. Ostraat, "Characterization of aln-based ceramic composites for use as millimeter-wave susceptor materials at high temperature: Dielectric properties of aln:mo with 0.25 vol% to 4.0 vol% mo from 25 to 550 °c," *Journal of Materials Research*, vol. 34, no. 15, 2019.
- [26] B. W. Hoff, F. W. Dynys, S. C. Hayden, R. O. Grudt, M. S. Hilario, A. E. Baros, and M. L. Ostraat, "Characterization of AlN-based ceramic composites for use as millimeter wave susceptor materials at high temperature: high temperature thermal properties of AlN:Mo with 0.25% to 4.0% Mo by volume," *MRS Advances*, pp. 1–12, 2019.

- [27] P. Kopyt and M. Celuch, “Coupled electromagnetic-thermodynamic simulations of microwave heating problems using the fdtd algorithm,” *Journal of Microwave Power and Electromagnetic Energy*, vol. 41, no. 4, pp. 18–29, 2007.
- [28] P. Kopyt and M. Celuch, “Modeling of microwave heating of foods,” in *Development of Packaging and Products for Use in Microwave Ovens* (M. Lorence and P. Pesheck, eds.), pp. 305–348, Woodhead Publishing, 2009.
- [29] T. Koutchma and V. V. Yakovlev, “Computer modeling of microwave heating processes for food preservation,” in *Mathematical Analysis of Food Processing* (M. Farid, ed.), pp. 625–657, CRC Press, 2010.
- [30] V. V. Yakovlev, S. M. Allan, M. L. Fall, and H. S. Shulman, “Computational study of thermal runaway in microwave processing of zirconia,” in *Microwave and RF Power Applications* (J. Tao, ed.), pp. 303–306, Cépaduès Éditions, 2011.
- [31] V. V. Yakovlev, *Introduction to Multiphysics Modeling in Microwave Power Engineering*, Short Course, IMPI’s 52nd Microwave Power Symposium, June 2018.
- [32] F. P. Incropera, D. P. Dewitt, T. L. Bergman, and A. S. Lavine, *Fundamentals of Heat and Mass Transfer*. John Wiley & Sons, Inc., 6th ed., 2007.
- [33] S. W. Churchill and H. H. Chu, “Correlating equations for laminar and turbulent free convection from a vertical plate,” *International Journal of Heat and Mass Transfer*, vol. 18, p. 1323–1329, 1975.